

# Water-in-olivine magma ascent chronometry: Every crystal is a clock

Megan E. Newcombe<sup>a,\*</sup>, Terry Plank<sup>b</sup>, Anna Barth<sup>b</sup>, Paul D. Asimow<sup>c</sup>, Erik Hauri<sup>d</sup>

<sup>a</sup> University of Maryland, College Park, MD 20742, USA

<sup>b</sup> Lamont-Doherty Earth Observatory, 61 Route 9W, Palisades, NY 10964, USA

<sup>c</sup> Division of Geological and Planetary Sciences, California Institute of Technology, 1200 E. California Blvd., Pasadena, CA 91125, USA

<sup>d</sup> Department of Terrestrial Magnetism, Carnegie Institution of Washington, 5241 Broad Branch Road, NW Washington, DC 20015, USA

## ARTICLE INFO

### Article history:

Received 18 September 2019

Received in revised form 25 March 2020

Accepted 31 March 2020

Available online 4 April 2020

## ABSTRACT

The syneruptive decompression rate of basaltic magma in volcanic conduits is thought to be a critical control on eruptive vigor. Recent efforts have constrained decompression rates using models of diffusive water loss from melt embayments, olivine-hosted melt inclusions and clinopyroxene phenocrysts; however, these techniques are difficult to apply because of the rarity of pyroxene crystals or melt embayments suitable for analysis and the complexities associated with modeling water loss from melt inclusions. We have developed a new magma ascent chronometer based on syneruptive diffusive water loss from olivine phenocrysts.

We have found water zonation in every olivine phenocryst we have measured, from explosive eruptions of Segouam, Fuego, Kilauea and Cerro Negro volcanoes. The majority of the olivine phenocrysts were polished to expose a central plane normal to the crystallographic 'b' axis and volatile concentration profiles were measured along 'a' and 'c' axes by secondary ion mass spectrometry (SIMS). Profiles are compared to 1D and 3D finite-element models of diffusive water loss from olivine, whose boundaries are in equilibrium with a melt undergoing closed-system degassing.

Least-squares fitting of measured water concentration gradients in olivine to a 1D Monte Carlo model produces constraints on magma decompression rates that are in good agreement with independent constraints from melt embayment studies and modeling of water loss from olivine-hosted melt inclusions at Fuego, Segouam, Kilauea, and Cerro Negro. Such agreement confirms the accuracy and sensitivity of the water-in-olivine chronometer over a range of decompression rates ( $dP/dt$ ) spanning ~2 orders of magnitude (from 0.007 to 0.45 MPa/s). We find that the assumption of a zero-water boundary condition (in which the water concentration at the edges of the olivine phenocrysts is fixed at 0 ppm throughout their ascent) leads to an overestimation of the decompression rate by an order of magnitude compared to the closed-system degassing boundary condition assumed in our model, thereby highlighting the sensitivity of the water-in-olivine chronometer to the host magma degassing path.

At Segouam, a wide range of best-fit values of  $dP/dt$  is obtained both from the water-in-olivine chronometer (0.04–0.23 MPa/s) and from melt embayments (0.02–0.13 MPa/s). We find systematically higher  $dP/dt$  values in the melt embayments that appear to have stalled or crystallized at the shallowest depths. Together, these observations are suggestive of magma acceleration during ascent.

A strength of the water-in-olivine chronometer is the prevalence of olivine in mafic to intermediate magmas. This new technique yields many values of  $dP/dt$  from a single eruption, providing insight into the diversity of ascent records carried by the crystal cargo and possibly defining changes in  $dP/dt$  through time and space. This data density offers a more detailed window into syneruptive conduit processes than has been possible using other techniques for constraining  $dP/dt$ . In theory, each crystal is a clock, with the potential to record variable ascent in the conduit, over the course of an eruption, between eruptions, and among volcanic systems.

© 2020 Elsevier B.V. All rights reserved.

## 1. Introduction

During the seconds to hours preceding a volcanic eruption, the rise of magma through the crust to the surface is accompanied by a

multitude of rapid physical and chemical changes. Decompression of magma during ascent reduces the solubility of volatile species in silicate melt, leading to exsolution of a vapor phase, which in turn drives acceleration of the ascending magma. This positive feedback may be countered to some extent by degassing-driven crystallization, which increases the viscosity and density of the magma. Syneruptive interactions between silicate liquid, crystals and vapor bubbles drive complex

\* Corresponding author.

E-mail address: [newcombe@umd.edu](mailto:newcombe@umd.edu) (M.E. Newcombe).

and non-linear changes in magma rheology, and are expected to exert a strong control on eruptive style (Gonnermann and Manga, 2007; Edmonds, 2008; Cassidy et al., 2018). Many models of varying complexity have been developed to ascertain the chemical and physical evolution of syneruptive magmas in volcanic conduits (Sparks, 1978; Wilson and Head, 1981; Mastin and Ghiorso, 2000; Llewellyn and Manga, 2005; Proussevitch and Sahagian, 2005; Suckale et al., 2010; Huber et al., 2014; La Spina et al., 2015). These models necessarily make many simplifying assumptions and their accuracy when applied to complex natural systems is hard to assess.

Petrologic techniques that use chemical signatures in erupted products to retroactively infer pre-eruptive decompression histories of magma are a promising approach to constraining conduit conditions and processes. Existing techniques for estimating magma ascent rates have exploited short-lived radioisotopes (Berlo et al., 2004; Turner et al., 2004), amphibole breakdown rims (Rutherford and Devine, 2003), number densities of bubbles and microlites (Toramaru, 2006; Toramaru et al., 2008), and concentration gradients across silicate minerals and glasses of rapidly-diffusing volatile species such as Li (Berlo et al., 2004) and water (Humphreys et al., 2008; Lloyd et al., 2013; Le Voyer et al., 2014; Lloyd et al., 2016; Myers et al., 2016; Myers et al., 2018).

The majority of the above listed magma ascent studies have focused on silicic systems. Recently developed magma ascent chronometers that exploit volatile concentration gradients along olivine-hosted melt embayments (Lloyd et al., 2014; Ferguson et al., 2016), water concentration gradients in clinopyroxene crystals (Lloyd et al., 2016) and trends of water loss from olivine-hosted melt inclusions of different sizes (Chen et al., 2013; Barth et al., 2019b) have extended magma ascent chronometry to mafic systems. Existing studies of magma ascent chronometry in mafic to intermediate systems have found a correlation between mass eruption rate and magma decompression rate (Ferguson et al., 2016; Barth et al., 2019b). These chronometers are providing insights into conduit conditions in the seconds to hours preceding eruption; however, challenges associated with their implementation (e.g., rarity of suitable samples) mean that existing studies of mafic to intermediate systems rely on a small number of independent constraints of magma decompression rate to characterize each eruption.

In this study, we explore the potential of water concentration gradients in olivine phenocrysts as records of syneruptive magma decompression. Olivine is a common phase in basaltic and intermediate systems, so a magma decompression chronometer based on water in olivine could potentially be applied to a broad range of eruptive deposits. In theory, many olivine phenocrysts could be characterized from a single eruptive deposit, providing more statistically robust estimates of magma decompression rates than previously possible. In practice, however, there are some challenges associated with this approach. One such challenge is that olivine is a nominally anhydrous mineral that incorporates only trace amounts of water in its structure (Bell and Rossman, 1992). The partition coefficient describing the equilibrium distribution of water between olivine and silicate melt [ $K_d$  = water in olivine (wt %) / water in melt (wt %)] is both small ( $\sim 0.001$ ) and uncertain (Fig. 1), such that an olivine phenocryst in equilibrium with a typical arc basalt containing  $\sim 4$  wt% water (Plank et al., 2013) is expected to contain only  $\sim 40$  ppm water (incorporated into the olivine structure as protons, but calculated and described hereafter as equivalent  $H_2O$  molecules by weight). Olivine phenocrysts in magmas that have degassed on ascent are expected to contain water concentration gradients from core to rim, with core concentrations containing up to a few 10s of ppm water and rim concentrations approaching zero ppm water, so characterization of syneruptively generated water concentration gradients in olivine phenocrysts requires analytical techniques that are capable of resolving water quantities and variations on the order of  $\sim 1$  ppm. This capability has been demonstrated in previous studies that used FTIR to analyze water concentration gradients in xenolithic olivine grains (Demouchy et al., 2006; Peslier and Luhr, 2006; Peslier et al., 2015),

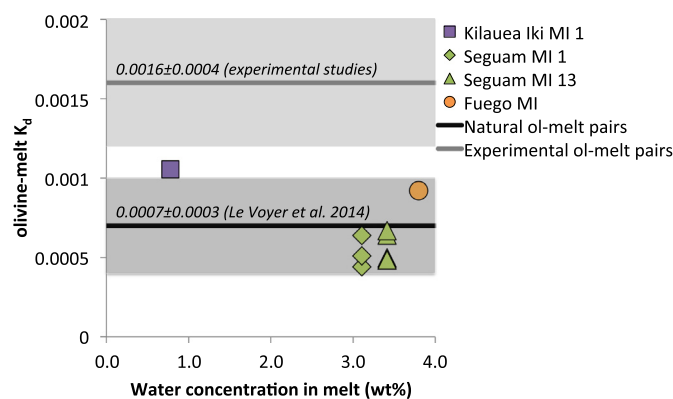


**Fig. 1.** Compilation of measured partition coefficients ( $K_d$ ) describing the equilibrium distribution of water between olivine and silicate melt (Le Voyer et al., 2014).  $K_d$  values determined from high-pressure experiments (Koga et al., 2003; Aubaud et al., 2004; Hauri et al., 2006; Tenner et al., 2009) are higher on average than  $K_d$  values determined by measurement of water in olivine-melt inclusion pairs (this study; Le Voyer et al., 2014). Gray shaded regions indicate one standard deviation of measured values; colored symbols are values determined by measurement of olivine-melt inclusion pairs in phenocrysts from Segum, Kilauea and Fuego volcanoes in this study.

nanoSIMS to analyze water zonation around olivine-hosted melt inclusions (Le Voyer et al., 2014), and SIMS to analyze water in olivine phenocrysts (Ferriss et al., 2018).

An additional challenge of using water in olivine as a magma ascent chronometer is that mechanisms and rates of water transport in olivine are complex. Water is incorporated in the olivine structure as protons that must be charge balanced by defects in the crystal structure; e.g.,  $Mg^{2+}$  vacancies can accommodate up to two protons and  $Si^{4+}$  vacancies can incorporate up to four protons. Proton diffusion through the olivine structure can then be charge balanced either via the migration of Mg and Si vacancies (hereafter referred to as the proton-vacancy mechanism, PV), or via reduction of  $Fe^{3+}$  defects (hereafter referred to as the redox or proton-polaron mechanism, PP). Proton diffusion by the PV mechanism is anisotropic with faster diffusion along the 'c' crystallographic axis than the 'a' and 'b' axes (note that Fig. 2 illustrates the relationship between olivine morphology and the three crystallographic axes; we will refer to these axes as 'a', 'b', and 'c', or equivalently as [100], [010], and [001]), and proton diffusion by the PP mechanism is anisotropic with faster diffusion along the 'a' axis than the 'b' and 'c' axes (Fig. 3; Kohlstedt and Mackwell, 1998; Ferriss et al., 2018). The availability and mobility of defects in olivine that can accommodate protons is dependent on olivine composition, temperature, pressure, and oxygen fugacity (Kohlstedt and Mackwell, 1998; Demouchy and Mackwell, 2006; Ferriss et al., 2018). Despite this underlying complexity, dehydration experiments on natural olivine phenocrysts from Kilauea and Cerro Negro volcanoes have demonstrated that the behavior of water in olivine during dehydration can be adequately described using relatively simple Arrhenius relationships (Fig. 3), and that the diffusion of water in dehydrating olivine phenocrysts is fastest along the crystallographic 'a' direction with a rate that lies between that expected for the PP and PV mechanisms (Ferriss et al., 2018; Barth et al., 2019b). Recent experimental work also supports a relationship between the rate of olivine dehydration and the forsterite content of the olivine, with lower forsterite olivines displaying higher diffusivities at a given temperature than higher forsterite olivines (Barth et al., 2019b).

The analytical, experimental and theoretical advances described above have paved the way for the development of a new magma ascent chronometer based on water diffusion in olivine phenocrysts. In the following sections, we describe protocols for phenocryst selection, analysis of water in olivine by SIMS, and numerical methods for constraining syneruptive magma decompression rates using water concentration gradients in olivine.

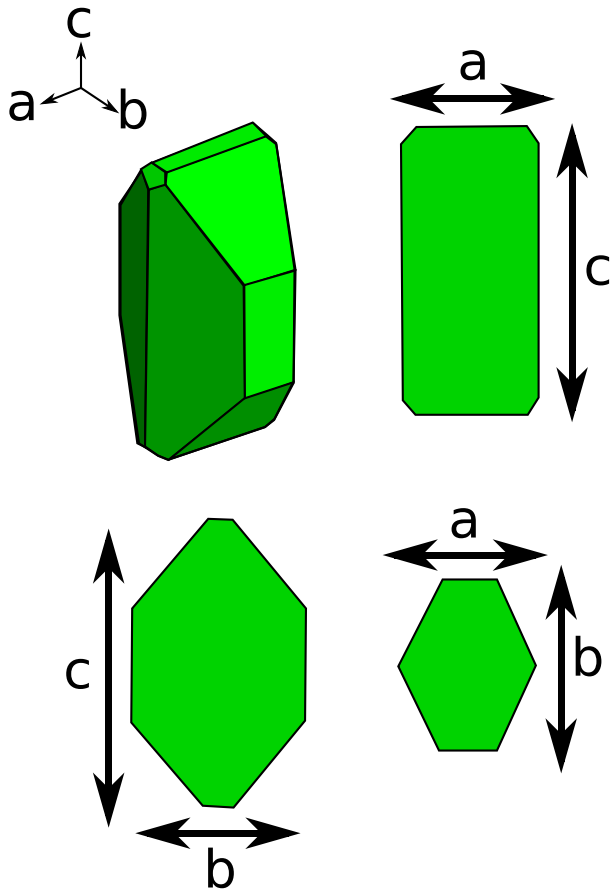


**Fig. 2.** Schematic of idealized 3D olivine morphology and shapes of 2D sections along the 'a'-'c', 'a'-'b', and 'b'-'c' planes. (Modified after Zussman et al. (1992) and Shea et al. (2015).)

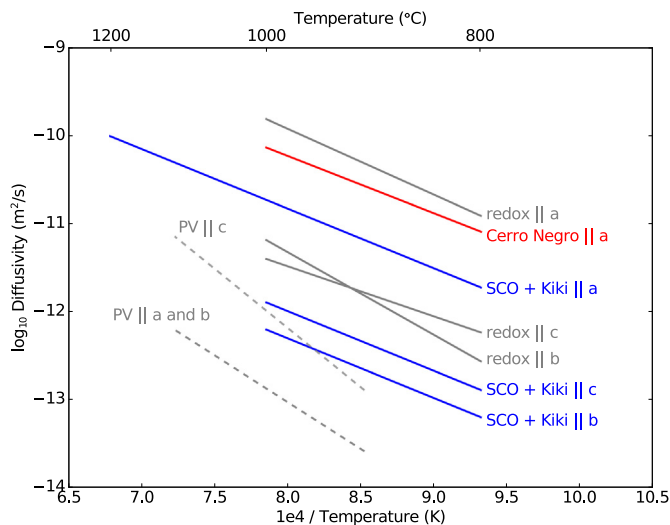


**Fig. 3.** Arrhenius plot showing the temperature dependence of experimentally determined diffusivities of water in olivine. 'PV' refers to the mobility of water via the proton vacancy mechanism (Kohlstedt and Mackwell, 1998; Demouchy and Mackwell, 2006), and 'redox' refers to the mobility of water via the proton polaron (PP) mechanism (Kohlstedt and Mackwell, 1998). Recent experimental dehydration experiments on natural olivine crystals [San Carlos olivine (SCO), phenocrysts from the 1959 Kilauea Iki eruption (Kiki), and phenocrysts from Cerro Negro volcano in Nicaragua] demonstrate that syneruptive water loss from olivine phenocrysts is fastest along the crystallographic 'a' axis, and the diffusivity of water along 'a' lies between rates expected for the PP and PV mechanisms (Ferriss et al., 2018; Barth et al., 2019b).

## 2. Samples

Olivine phenocrysts were selected from tephra erupted during the subplinian 1974 eruption of Fuego volcano; the 1977 fire-fountain eruption of Segum volcano; episode 1 of the 1959 Kilauea Iki fire-fountain eruption; and the 1992 explosive and 1995 explosive/effusive eruptions of Cerro Negro. These samples were selected primarily because their syneruptive ascent histories have been previously constrained using volatile concentration gradients in melt embayments (Lloyd et al., 2014; Ferguson et al., 2016), volatile loss from olivine-hosted melt inclusions (Lloyd et al., 2013; Barth et al., 2019b), and concentration gradients of water preserved in clinopyroxene phenocrysts (Lloyd et al., 2016). Further details of the studied eruptions are provided below and in Table 1.

### 2.1. Samples from the October 1974 eruption of Volcán de Fuego (Guatemala)

Volcán de Fuego erupted  $\sim 0.1 \text{ km}^3$  of porphyritic, high-alumina basalt in a series of four distinct subplinian events between 14 and 23 October 1974 (Rose et al., 1978; Rose et al., 2008). Previous studies of olivine-hosted melt inclusions from this eruption indicate that the pre-eruptive magma contained  $\sim 4 \text{ wt\% H}_2\text{O}$  (Sisson and Layne, 1993; Roggensack, 2001; Berlo et al., 2012; Lloyd et al., 2013) and that the onset of olivine crystallization in the Fuego magma occurred at depths of  $\sim 10\text{--}22 \text{ km}$  (Lloyd et al., 2013; Lloyd et al., 2014; Moore et al., 2015).

We selected five olivine phenocrysts from the same airfall ash samples studied by Lloyd et al. (2013, 2014, 2016). These samples erupted on 17th October 1974, and were collected during the eruption by S. Bonis of the Instituto Geográfico Nacional, Guatemala City and provided by William Rose (IGSN: ASL000001 and ASL000002). Olivine phenocrysts from this phase of the eruption range in composition from Fo<sub>72</sub> to Fo<sub>78</sub> (Lloyd et al., 2013).

The 17th October event had a volcanic explosivity index (VEI) of 4 and its eruptive column is estimated to have reached a height of  $\sim 15 \text{ km}$  (Rose et al., 1978). The average decompression rate of magma erupted during the 17th October subplinian event was estimated by modeling the generation of volatile concentration gradients in four olivine-hosted melt embayments. The H<sub>2</sub>O, CO<sub>2</sub> and S profiles in four embayments yielded decompression rates from 0.3 to 0.5 MPa/s, implying that magma ascended from its crystallization depth to the surface over a time period of 8–12 min at a velocity of 11–17 m/s (Lloyd et al., 2014).

### 2.2. Samples from the 1977 eruption of Segum volcano (central Aleutian arc)

On 6–8 March 1977, the US Coast Guard observed 8 lava fountains reaching heights of  $\sim 90 \text{ m}$  erupting from a  $\sim 1 \text{ km}$ -long radial rift on Segum volcano, also known as Pyre Peak (Miller et al., 1998). The eruption is estimated to have produced  $\sim 0.06 \text{ km}^3$  of basaltic material (Jicha and Singer, 2006), including tephra and lava flows (this volume is based on stratigraphic analysis of present-day deposits). The maximum VEI of the 1977 eruption is estimated to be 1 ([www.avo.alaska.edu](http://www.avo.alaska.edu)).

We selected seven olivine phenocrysts from a rapidly quenched basaltic tephra sample (sample SEG-07-06 of Zimmer et al., 2010). Melt inclusions from this sample were previously reported to contain  $3.3 \pm 0.33 \text{ wt\%}$  water and their olivine hosts have compositions that range from Fo<sub>80</sub> to Fo<sub>85</sub> (Zimmer et al., 2010). Lloyd et al. (2016) report water concentrations of clinopyroxene phenocrysts and associated melt inclusions from tephra sample SEG-07-06 and from a coevally erupted lava flow, from which they developed a model of post-eruption water loss from the lava samples during slow cooling; however, syneruptive magma ascent rates have not yet been determined for this eruption. Here, we report new constraints on magma ascent rates for the 1977 eruption of Segum volcano, based on both modeling

**Table 1**  
Characteristics of studied eruptions and olivine phenocrysts from each eruption that were selected for analysis.  $dP/dt$  values are median estimates of decompression rates derived by modeling volatile loss from melt embayments (at Seguam, Kilauea Iki and Fuego) or water loss from olivine-hosted melt inclusions (at Cerro Negro). MER is mass eruption rate, which is derived either from estimates of total volume and duration or from plume height (either from direct observation or from dispersal mapping). VEI is the volcano explosivity index. Sources of ascent duration, MER and VEI values are provided in the following references: 1. Barth et al. (2019b); 2. Lloyd et al. (2016); 3. Ferguson et al. (2016); and 4. Lloyd et al. (2014).

Eruption	$dP/dt$ (MPa/s)	Ascent duration (h)	$\log_{10}MER$	VEI	References	Forsterite content
Cerro Negro 1992	0.007	3	5.0	3	1	78–82
Cerro Negro 1995	0.001	15	4.1	2	1	82
Seguam 1977	0.07	1.6	5.5	1	2, this study	80–85
Kilauea Iki 1959	0.05	0.6	5.9	2	3	86
Fuego 1974	0.38	0.2	6.5	4	4	72–78

of volatile concentration gradients in four olivine-hosted melt embayments and on modeling of water concentration gradients measured across olivine phenocrysts.

### 2.3. Samples from episode 1 of the 1959 Kilauea Iki eruption (Hawaii)

This archetypal “Hawaiian-style” fire-fountain eruption began on November 14, 1959, and its 17 eruptive episodes spanned a total of 36 days (Richter et al., 1970). Each eruptive episode began with a phase of lava fountaining and coeval filling of a lava lake, followed by the cessation of fountaining and subsequent draining of the lava lake back into the vent (Eaton et al., 1987). For this reason, magma erupted during every eruptive episode after episode 1 suffered from mixing with lava that drained back into the vent during the previous eruptive episode (Eaton et al., 1987; Wallace and Anderson Jr., 1998; Sides et al., 2014). In this study, we focus on tephra from episode 1 of the eruption, which was unaffected by lava drainback, thereby avoiding potential complexities in the ascent histories of magmas that have mixed with degassed and cooled drainback lava in the conduit. Fire fountains from episode 1 of the Kilauea Iki eruption reached a maximum height of ~380 m and produced  $\sim 30 \times 10^6 \text{ m}^3$  of lava over seven days (Richter et al., 1970; Eaton et al., 1987). This event is assigned a VEI of 2.

We selected one olivine phenocryst (Kilauea\_Iki\_ol2; IGSN: IEMN1KIO2) from tephra layer p17 of Stovall et al. (2011). Tephra from this layer is relatively coarse, with a mean maximum clast size of ~55 mm (Stovall et al., 2011). Ferguson et al. (2016) used volatile concentration gradients along an olivine-hosted melt embayment from this sample to constrain a magma decompression rate of  $\sim 0.05 \pm 0.005 \text{ MPa/s}$  from 110 MPa (~4 km depth) during episode 1 of the Kilauea Iki eruption, corresponding to an ascent duration of ~36 min at an average velocity of ~2 m/s.

#### 2.3.1. Samples from the 1992 and 1995 eruptions of Cerro Negro

The 1992 eruption of Cerro Negro volcano, Nicaragua, began at 23:45 on April 9th with an explosive paroxysm that lasted until 16:05 on April 12th. This VEI 3 explosive eruption generated a 7 km ash cloud and produced a tephra volume of  $0.011 \text{ km}^3$  (McClelland, 1992).

We selected two olivine phenocrysts from a basaltic sample of proximal ash and lapilli that was collected on April 13th, 0.5 km NW of the Cerro Negro vent, by Gerardo Soto (IGSN: IEACB0005). The sampled tephra is thought to represent the late stages of the paroxysmal activity. Melt inclusions from this sample contain up to ~4.7 wt% water and their olivine hosts have compositions that range from  $\text{Fo}_{71.5}$  to  $\text{Fo}_{82}$  (Barth et al., 2019b). Barth et al. (2019b) used a model of water loss from olivine-hosted melt inclusions to constrain a magma decompression rate of  $\sim 0.007 \text{ MPa/s}$  from a depth of ~15 km, corresponding to an ascent duration of ~7 h at an average velocity of ~0.3 m/s.

The 1995 eruption of Cerro Negro volcano began on November 19th and lasted until December 2nd. This VEI 2 eruption generated a 2–3 km high ash cloud and produced  $0.0013 \text{ km}^3$  of tephra (most of which was generated during the last four days of the eruption) and  $0.0037 \text{ km}^3$  of lava (Hill et al., 1998). The major and trace element composition of the 1995 magma is nearly identical to the 1992 magma (Hill et al., 1998; Barth et al., 2019b).

We selected one olivine phenocryst from a sample of ash (CN16ACB\_3) collected in August 2016, on the western edge of the Cerro Negro cone, by Anna Barth and Armando Saballos (IGSN: IEACB0003). Melt inclusions from this sample contain up to ~4.7 wt% water and their olivine hosts have compositions that range from  $\text{Fo}_{71.5}$  to  $\text{Fo}_{82}$  (Barth et al., 2019b). Barth et al. (2019b) used a model of water loss from olivine-hosted melt inclusions to constrain a magma decompression rate of  $\sim 0.001 \text{ MPa/s}$  from a depth of ~15 km, corresponding to an ascent duration of ~40 h at an average velocity of ~0.05 m/s.

## 3. Methods

### 3.1. Selection and preparation of olivine phenocrysts for analysis

Fine-grained tephra from each target eruption were picked for olivine phenocrysts using a binocular microscope. In selecting phenocrysts for analysis, we looked for crystals that appeared to be unbroken (as evidenced by a full coating of vesicular glass and well-developed crystal facets) with distinctive crystal morphology that allowed identification of crystallographic orientation (Zussman et al., 1992; Fig. 2). The olivine phenocrysts were selected for optical clarity, avoiding the presence of melt inclusions. Each olivine phenocryst was oriented parallel to one of its crystallographic axes (orientations determined by crystal morphology were later checked by electron backscatter diffraction) before being mounted in an individual dental resin plug, ground down to its approximate midpoint and polished to  $0.25 \mu\text{m}$  using diamond suspensions. After polishing, the crystals were removed from the dental resin plugs; cleaned in ultrasonic baths of toluene, acetone and isopropanol; baked in a vacuum oven at ~110 °C for several days; and pressed into indium mounts.

### 3.2. Analysis of volatiles and phosphorus in olivine and melt inclusions by SIMS

Concentrations of volatiles ( $\text{H}_2\text{O}$ ,  $\text{CO}_2$ , S, Cl, F) and P were characterized using the Cameca IMS 6f ion microprobe at the Department of Terrestrial Magnetism, Carnegie Institute of Washington, following previously developed analytical protocols (Hauri, 2002; Koga et al., 2003; Mosenfelder et al., 2011; Kumamoto et al., 2017). Samples were coated with a ~40–80-nm layer of gold and placed into the evacuated sample exchange chamber of the SIMS one to three days prior to the beginning of the analytical session. The  $\text{Cs}^+$  primary beam was tuned to achieve an approximate beam diameter of ~20  $\mu\text{m}$  and a current of ~15–20 nA, with charge compensation provided by an electron flood gun. Prior to data collection, the sample area was pre-sputtered for 120 s with the rastered primary beam in order to remove the gold coat and surface contamination. During data collection, a field aperture was used to ensure the collection of ions from only the central ~10  $\mu\text{m}$  of the measurement area. Negatively charged  $^{12}\text{C}^-$ ,  $^{16}\text{O}^1\text{H}^-$ ,  $^{19}\text{F}^-$ ,  $^{30}\text{Si}^-$ ,  $^{31}\text{P}^-$ ,  $^{32}\text{S}^-$  and  $^{35}\text{Cl}^-$  ions were detected using an electron multiplier detector. The mass resolving power was sufficient to resolve  $^{16}\text{O}^1\text{H}^-$  from  $^{17}\text{O}$ . Five cycles of data were collected at each point. Occasionally, an electrical glitch would result in one or more cycles recording zero



counts of one or more masses; these 'empty' cycles were deleted prior to further data reduction.

Data reduction and calibration were approached following a protocol similar to that described by Kumamoto et al. (2017). A selection of basaltic glasses and grains of olivine and orthopyroxene with well-characterized volatile contents were used as standards (see Supplementary data). We note that calibrations of absolute water concentrations in olivine are currently subject to uncertainties of ~30 rel. % due to uncertainties in the absorption coefficients used to measure the water concentrations of the standards by FTIR (Bell et al., 2003; Withers et al., 2012); the calibrations of water concentration in olivine used in this study are based on absolute water concentrations of mineral standards determined by Bell et al. (2003). Note that the decompression rates we obtain are completely insensitive to this source of systematic uncertainty in the water concentrations, because the partition coefficients used in the modeling were calibrated using the same means of measuring H<sub>2</sub>O in olivine. Counts of volatile and <sup>31</sup>P<sup>−</sup> ions were first divided by counts of <sup>30</sup>Si<sup>−</sup> in order to account for instrumental drift (e.g., caused by fluctuations in primary beam current) and multiplied by SiO<sub>2</sub>/50 (where SiO<sub>2</sub> is the independently measured silica concentration of the sample in wt%). The detection limit (as defined by Long and Winefordner, 1983) for analyses of water in olivine was calculated using replicate analyses of "Suprasil" glass containing <0.5 ppm H<sub>2</sub>O, and was found to be <4 ppm H<sub>2</sub>O in all analytical sessions (this estimate is an upper bound, given the non-zero water concentration of Suprasil glass and the fact that the quality of the vacuum improved over the course of each session). Note that data for Kilauea-Iki-ol2 (IGSN: IEMN1K10) was presented previously by Ferriss et al. (2018). The water calibration used in this study differs slightly to that used by Ferriss et al. (2018) (differences include the application in this study of a correction for instrumental drift and multiplication of the <sup>16</sup>O<sup>1</sup>H/<sup>30</sup>Si ratio by SiO<sub>2</sub>/50), resulting in a shift in water concentrations by ~1 ppm.

### 3.3. Analysis of volatiles along melt embayments by nanoSIMS

Concentrations of volatiles (H<sub>2</sub>O, CO<sub>2</sub>, S, Cl, F) along five melt embayments from Segum volcano were characterized using the Cameca NanoSIMS 50L at the Department of Terrestrial Magnetism, Carnegie Institute of Washington, following previously developed analytical protocols (Hauri et al., 2002; Hauri et al., 2011; Lloyd et al., 2014; Ferguson et al., 2016). Samples were placed into the sample exchange chamber of the nanoSIMS one to three days prior to the beginning of the analytical session. The Cs<sup>+</sup> primary beam was tuned to achieve an approximate beam diameter of ~5 μm and a current of ~4 nA, with charge compensation provided by an electron flood gun. Prior to data collection, the sample area was pre-sputtered for 120 s in order to remove the gold coat and surface contamination. The primary beam was rastered over a 10 × 10 μm area. During data collection, electronic gating was applied to ensure the collection of ions from only the inner 14% of the measurement area (corresponding to an area of 3.7 × 3.7 μm). Negatively charged <sup>12</sup>C<sup>−</sup>, <sup>16</sup>O<sup>1</sup>H<sup>−</sup>, <sup>19</sup>F<sup>−</sup>, <sup>30</sup>Si<sup>−</sup>, <sup>32</sup>S<sup>−</sup> and <sup>35</sup>Cl<sup>−</sup> ions were detected simultaneously using six electron multipliers. <sup>30</sup>Si<sup>−</sup> was used as a denominator of all reported ion intensity ratios, and the mass resolving power was sufficient to resolve <sup>16</sup>O<sup>1</sup>H<sup>−</sup> from <sup>17</sup>O. A selection of basaltic and basaltic andesitic glasses with well-characterized major element and volatile contents were used as standards (see Supplementary data). 35 replicate analyses of basaltic andesite in-house standard glass MR:ND-70-01 yielded relative standard deviations (100 × standard deviation / mean) of 4.4% for CO<sub>2</sub>, 4.5% for H<sub>2</sub>O, 2.8% for F, 6.0% for S, and 16.1% for Cl (analyses and accepted values for these standards are provided in the Supplementary data tables).

### 3.4. Analysis of major, minor, and trace elements by electron microprobe

Olivine phenocrysts were analyzed for major, minor, and trace elements using a Cameca SX100 microprobe (EMP) at the American Museum of Natural History (AMNH). The olivine phenocrysts were analyzed using a 10 nA beam current and a 15 kV accelerating potential with a focused beam (nominal beam diameter ~1 μm). On-peak counting times for major elements varied between 20s (Mg, Si, Ca, Mn, Al, Fe), and 40s (Ti and P). Background counting times for the elements were set to 50% of their on-peak counting times. All analyses were corrected for inter-run calibration offsets using factors determined by replicate analyses of San Carlos olivine. Raw data, corrected data, and correction factors are provided in the Supplementary data tables. Replicate analyses of San Carlos olivine yielded average 2 RSDs of <3% for SiO<sub>2</sub>, FeO, and MgO.

### 3.5. Estimation of syneruptive magma decompression rates at Segum using volatile concentration gradients in melt embayments

Concentration gradients of volatiles along olivine-hosted melt embayments have been used to constrain syneruptive magma decompression rates of magmas at Kilauea and Fuego volcanoes by Ferguson et al. (2016) and Lloyd et al. (2014). Here, we apply the methods of Ferguson et al. (2016) and Lloyd et al. (2014) to constrain the syneruptive decompression rate of magma during the 1977 eruption of Segum volcano. We constructed a one-dimensional, finite-element diffusion model to calculate the evolution of volatile concentrations (H<sub>2</sub>O, CO<sub>2</sub>, and S) along the length of olivine-hosted melt embayments from Segum during magma ascent and degassing. This model adopts the melt-composition- and water-concentration-dependent water diffusivity of Ni and Zhang (2018). The diffusivities of CO<sub>2</sub> and S in the melt are both assumed to be functions of water concentration (Zhang et al., 2007). We assume a constant temperature of 1070 °C for this calculation, based on the application of the olivine-liquid thermometer of Sugawara (2000) with a correction to account for the effect of water on the olivine liquidus temperature (Médard and Grove, 2008). We impose an equilibrium degassing boundary condition at the exterior end of the embayments (all of which terminate with a vapor bubble) and we assume a no-flux boundary condition at the interior end of the embayments. The equilibrium degassing boundary condition (i.e., the expected evolution of concentrations of dissolved volatiles in melt in equilibrium with vapor as a function of pressure) is calculated for H<sub>2</sub>O and CO<sub>2</sub> using VolatileCalc (Newman and Lowenstern, 2002). We constrain the evolution of S in the magma during decompression by fitting an exponential function [S (ppm) = 53.8 exp (0.767 × H<sub>2</sub>O (wt%))] through our H<sub>2</sub>O-S melt inclusion data, and then relating S concentration to pressure via the H<sub>2</sub>O-pressure relationship calculated using VolatileCalc. We note that the SolEx model of Witham et al. (2012) allows the calculation of H<sub>2</sub>O, CO<sub>2</sub>, and S concentrations in decompressing magmas undergoing open- or closed-system degassing. We attempted to fit the embayments using a degassing boundary condition calculated by SolEx, but we found that the delayed degassing of S predicted by this model (which is not supported by our H<sub>2</sub>O-S melt inclusion data) was unable to reproduce the measured H<sub>2</sub>O and S concentration gradients in the embayments. Initially, we made the assumption that the Segum magma underwent closed-system degassing with 0 wt% pre-existing vapor in the melt; however, upon comparing our model output to the measured volatile concentration gradients in the Segum embayments, we found that several embayments have CO<sub>2</sub> concentrations that are elevated above values expected by this model. Instead, we found that we were able to more faithfully reproduce the concentrations of H<sub>2</sub>O, S, and CO<sub>2</sub> in the interiors of the embayments if we assumed some amount (from 1 to 5 wt%) of pre-existing vapor in the melt prior to ascent. This pre-existing vapor is rich in CO<sub>2</sub> and has the effect of slowing the loss of CO<sub>2</sub> from the melt to the vapor during decompression. We note that other authors have also suggested that fluxing of CO<sub>2</sub>-rich vapor

could be an important process at arc volcanoes (Blundy et al., 2010; Van Hinsberg et al., 2016; Caricchi et al., 2018).

The forward model described above was used to simulate the diffusion of H<sub>2</sub>O, CO<sub>2</sub>, and S along melt embayments during magma ascent and decompression. We used a least-squares minimization approach to find the initial pressure [ $P_0$  (MPa)] and magma decompression rate [ $dP/dt$  (MPa/s)] that produced the best fit to the observed volatile concentration gradients in the Seguam embayments (Fig. 4). In order to ensure that each volatile species (H<sub>2</sub>O, CO<sub>2</sub>, and S) was weighted approximately evenly during this fitting procedure, we divided the residuals between the model and the data by the maximum measured concentration of that species in the embayment. The minimization was executed using MATLAB function *fminsearch*.

### 3.6. Estimation of syneruptive magma decompression rates at Seguam, Fuego, Kilauea Iki and Cerro Negro using water concentration gradients in olivine

#### 3.6.1. One-dimensional Monte Carlo fitting procedure for water concentration gradients measured in olivine phenocrysts along their crystallographic 'a' axis

We have developed a one-dimensional (1D) Monte Carlo method that uses water concentration gradients along the crystallographic 'a'

axis in relatively inclusion-free olivine phenocrysts to constrain syneruptive magma decompression rates ( $dP/dt$ ). The olivine phenocrysts are assumed to ascend the volcanic conduit in a magma that is undergoing closed-system degassing (Newman and Lowenstern, 2002; Witham et al., 2012) from an initial magma volatile content for each eruption that is selected based on the highest measured H<sub>2</sub>O and CO<sub>2</sub> in olivine-hosted melt inclusions (Lloyd et al., 2013; Moore et al., 2015). The concentration of water in olivine in equilibrium with the degassing carrier magma is calculated using a constant partition coefficient ( $K_d$ ) (model parameters are compiled in Table 2). We apply a temperature-dependent diffusivity of water in olivine along the crystallographic 'a' axis ( $D_a$ ) that has been experimentally determined via dehydration of olivine phenocrysts with forsterite contents ( $\sim Fo_{79}$ ) similar to the Fuego, Seguam and Cerro Negro olivines considered here (Barth et al., 2019b). We make the simplifying assumptions that the magma decompresses at a constant rate and that magma ascent is isothermal. We also make the assumption that our olivine phenocrysts crystallized prior to the onset of water degassing from the magma (i.e., we assume that the widths of the phenocrysts remain constant throughout ascent). At each increment of decompression, water exsolves from the magma, resulting in a decrease in the water concentration at the external faces of the olivine phenocrysts and subsequent diffusion of water from the center to the edge of the olivine.

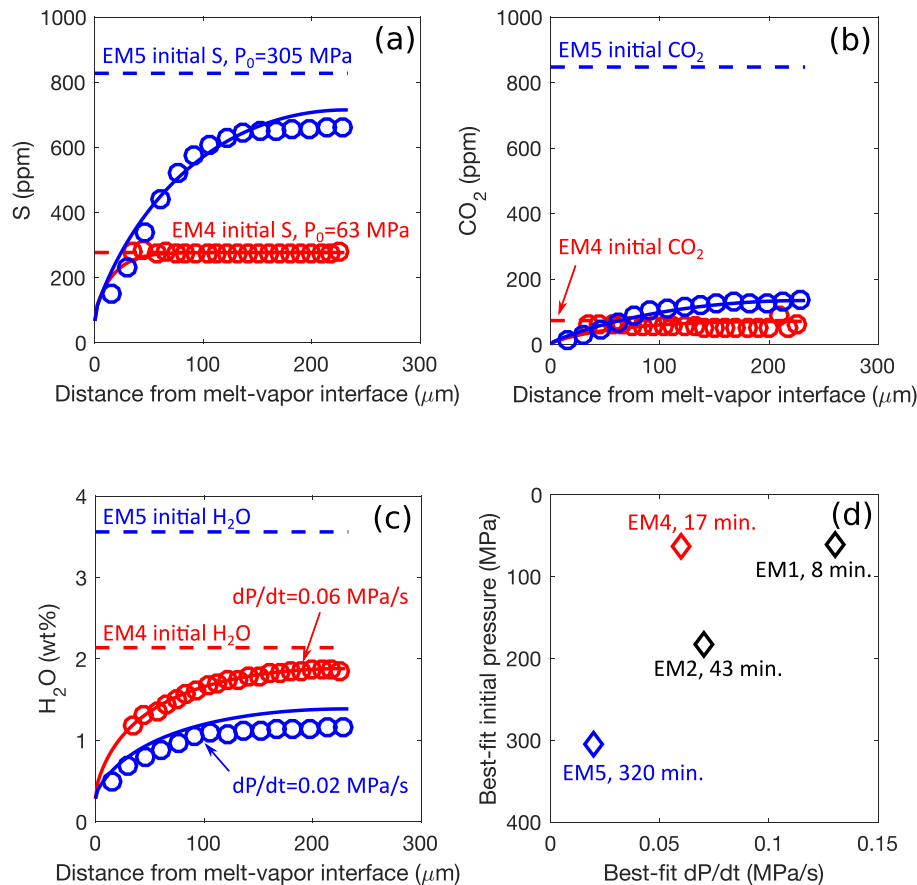


**Fig. 4.** Results of Seguam embayment fitting. (a) Measured and modeled S concentration gradients along Seguam embayments EM4 (in red) and EM5 (in blue). Concentrations are plotted against distance from the melt-vapor interface of the bubble at the outlet of each embayment. S is a slower diffusing species than H<sub>2</sub>O, so S concentrations in the embayments are more sensitive to changes in initial pressure than are H<sub>2</sub>O concentrations. The higher S concentration in EM5 compared to EM4 suggests that EM5 stalled or crystallized at a higher pressure than EM4 prior to its final ascent. (b) Measured and modeled CO<sub>2</sub> concentration gradients along Seguam embayments EM4 (in red) and EM5 (in blue). (c) Measured and modeled H<sub>2</sub>O concentration gradients along embayments EM4 (in red) and EM5 (in blue). Initial H<sub>2</sub>O concentrations assumed for the model (dashed lines) are calculated from the initial S concentrations in (a) using an exponential parameterization of the relationship between S and H<sub>2</sub>O defined by Seguam olivine-hosted melt inclusion compositions. H<sub>2</sub>O diffuses more rapidly than S, so H<sub>2</sub>O concentration gradients are more sensitive to changes in decompression rate than are S concentration gradients. The low H<sub>2</sub>O in the interior of EM5, despite the high S in the interior of this embayment, suggests that EM5 ascended more slowly than EM4. (d) Best-fit initial pressures and decompression rates of Seguam magma, obtained by fitting concentration gradients of H<sub>2</sub>O, S, and CO<sub>2</sub> along four olivine-hosted melt embayments. There is a negative correlation between initial pressure and decompression rate, suggestive of magma acceleration from the source region to the surface. Additional data and model fits are provided in the Supplementary information.

**Table 2**

Model input parameters. ' $K_d$  measured' refers to values of  $K_d$  determined by measurement of melt inclusion-olivine pairs (Fig. 1). References: 1. Barth et al. (2019b); 2. Moore et al. (2015); 3. Lloyd et al. (2016); 4. Ferguson et al. (2016); 5. Lloyd et al. (2014).

Eruption	Initial H <sub>2</sub> O (wt%)	Initial CO <sub>2</sub> (ppm)	Initial pressure (MPa)	Temperature (°C)	References	$K_d$ measured	$K_d$ range applied
Cerro Negro 1992	4.75	600	400	1100	1	N/A	0.0005–0.0009
Cerro Negro 1995	4.75	600	400	1100	1	N/A	0.0005–0.0009
Seguam 1977	4.20	900	320	1070	2, 3, this study	0.00055	0.0005–0.0009
Kilauea Iki 1959	0.78	400	50	1200	4	0.00105	N/A
Fuego 1974	4.30	4000	400	1030	2, 5	0.0009	0.0005–0.0009

The diffusion of water through the olivine is modeled using a finite-element, explicit scheme. Our 1D code is available on Github (DOI: <https://doi.org/10.5281/zenodo.3727149>).

The forward model described above can be used to calculate expected water concentration gradients along the 'a' axis in olivine phenocrysts that have ascended the volcanic conduit in a degassing magma at any given magma decompression rate (Fig. 5). The best-fit decompression rate for a given olivine phenocryst is determined by minimizing the misfit (the sum of the squares of the residuals divided by the number of

data points) between the modeled and measured water concentration gradients along 'a', using MATLAB function *fminsearch*.

There are several sources of uncertainty in our best-fit values of  $dP/dt$ . For example, estimates of magma temperature are commonly associated with uncertainties of 10's of degrees, and these temperature uncertainties translate to errors in the water diffusivity assumed for our model. Another source of error is uncertainty in the olivine-melt partition coefficient for water, for which a range of values has been reported (Fig. 1; Aubaud et al., 2004; Hauri et al.,

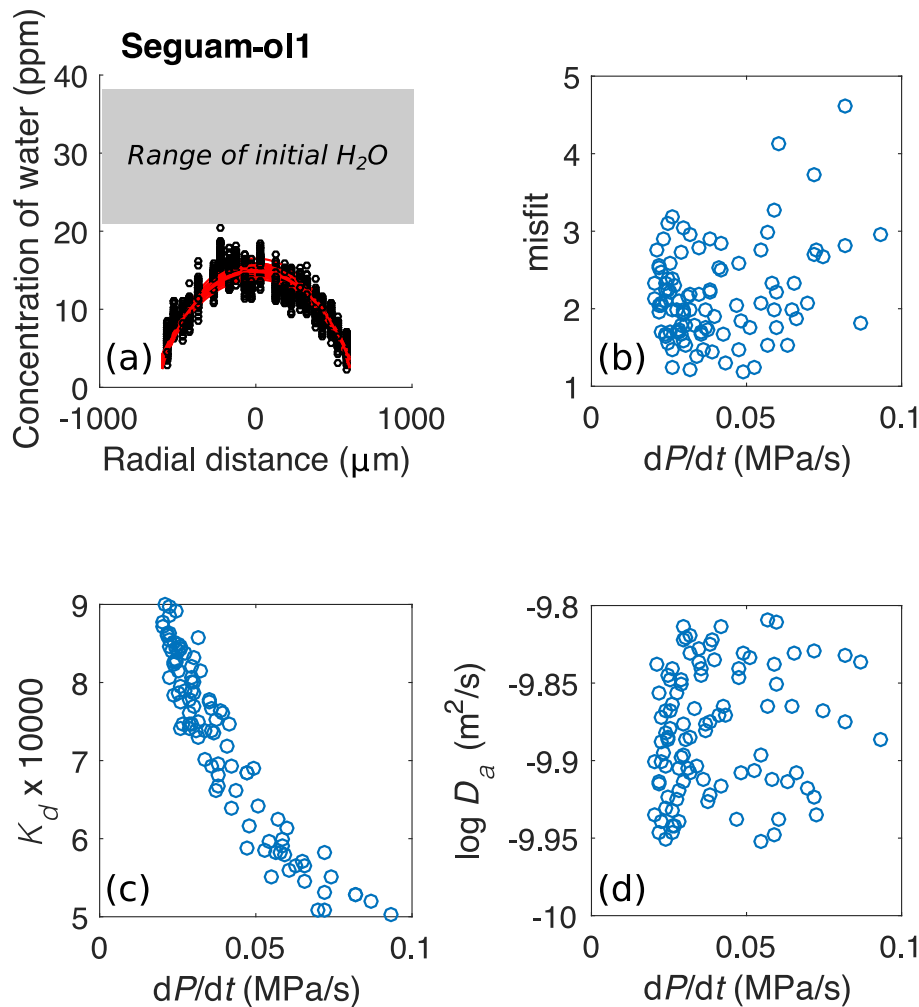


**Fig. 5.** Example of 1D Monte Carlo method for using water concentration gradients along the crystallographic 'a' axis in relatively inclusion-free olivine phenocrysts to invert for magma decompression rate ( $dP/dt$ ). (a) Synthetic SIMS data (black circles) and diffusion model fits (red curves) for Seguam-ol1. Synthetic water concentration profiles are generated by adding noise to our SIMS measurements, assuming that each data point is normally distributed with a mean corresponding to the measured value and a standard deviation of 1.09 ppm (based on replicate analyses of homogeneous Herasil glass; see Supplementary data tables). The initial water concentration of the olivine is calculated from the water concentration in the initial magma (based on the highest measured water concentration in the Seguam melt inclusion population) using a constant partition coefficient ( $K_d$ ) drawn from a uniform distribution (see panel (c)). The gray shaded region indicates the range of calculated initial water concentrations. (b) Best-fit values of  $dP/dt$  are determined by least-squares fitting of a 1D finite-element diffusion model to the synthetic water concentration profiles plotted in (a). The misfit is calculated as the sum of the squares of the residuals between the model and the synthetic data points, divided by the number of data points. Minimization of the misfit parameter (by varying  $dP/dt$ ) is performed by the MATLAB *fminsearch* function. (c) The value of  $K_d$  used in a given Monte Carlo simulation is drawn from a uniform distribution on the interval  $[5 \times 10^{-4}, 9 \times 10^{-4}]$ . There is a strong trade-off between  $K_d$  and  $dP/dt$ . (d) The value of  $\log_{10} D_a$  used in a given Monte Carlo simulation is drawn from a uniform distribution on an interval spanning a width that reflects a temperature uncertainty of  $\pm 20$  °C.

2006; Le Voyer et al., 2014; Adam et al., 2016). Additionally, there is an uncertainty associated with each of our SIMS measurements of water concentration; these measurement errors also contribute to uncertainties in our best-fit values of  $dP/dt$ . In order to assess the magnitude of the uncertainties associated with our best-fit  $dP/dt$  values, we have adopted a Monte Carlo approach: for each olivine phenocryst, we generate 100 synthetic water concentration profiles by adding Gaussian noise to the original data, with a standard deviation of 1.09 ppm (based on replicate analyses of homogeneous Herasil glass; see Supplementary data tables). The value of  $\log_{10}D_a$  used in a given Monte Carlo simulation is drawn from a uniform distribution on an interval spanning a width that reflects a temperature uncertainty of  $\pm 20$  °C. Similarly, the value of  $K_d$  used in a given Monte Carlo simulation is drawn from a uniform distribution on the interval  $[5 \times 10^{-4}, 9 \times 10^{-4}]$ . A summary of our input model parameters is provided in Table 2. At the completion of fitting our 100 synthetic water concentration profiles, we obtain 100 different 'best-fit' values of  $dP/dt$ . The spread in these best-fit values reflects the uncertainty in  $dP/dt$  imparted by measurement error and uncertainties in temperature and  $K_d$ . We report 'overall best-fit' values as the logarithmic mean of these 100 individual best fits and uncertainty as one standard deviation of best-fit  $\log_{10}dP/dt$  values determined by the Monte Carlo simulation. We note that there is a strong anti-correlation between  $K_d$  and  $dP/dt$  (Fig. 5c), and we consider uncertainty in  $K_d$  to be the largest source of uncertainty in our best-fit  $dP/dt$  values. High values of  $\log_{10}D_a$  should result in more rapid loss of water to the external magma during decompression-driven degassing, thereby requiring faster decompression rates to match the measured water concentration data; therefore, one expects to see a positive correlation between  $\log_{10}D_a$  and best-fit  $dP/dt$ . The weakness of this correlation in the Monte Carlo population suggests that the assumed  $\pm 20$  °C temperature error contributes a relatively minor source of uncertainty in our best-fit  $dP/dt$  values (Fig. 5d).

### 3.6.2. Three-dimensional forward modeling of anisotropic water diffusion in olivine phenocrysts

In order to check the validity of the 1D modeling approach described in Section 3.6.1, we have performed some forward model calculations of three-dimensional (3D), anisotropic water diffusion in olivine phenocrysts, using a modified version of the 3D model first presented by Le Voyer et al. (2014). This model constructs a rectangular prism of olivine on a Cartesian grid with 5- $\mu$ m node spacing and crystal faces oriented normal to the crystallographic 'a', 'b' and 'c' axes. The water concentration in the external magma is assumed to be spatially uniform, and the water concentration in the olivine adjacent to the external magma is calculated using a constant, user-defined value of  $K_d$ . The original model presented by Le Voyer et al. (2014) assumed a constant concentration of water in the external magma. We have modified this aspect of the original model to allow the external magma to evolve along a simple square root parameterization of closed system degassing relationships calculated by VolatileCalc (Newman and Lowenstern, 2002). We define the initial water concentration and pressure of the magma based on the highest measured  $H_2O$  and  $CO_2$  in olivine-hosted melt inclusions (Lloyd et al., 2013; Moore et al., 2015), and we assume that the host magma undergoes decompression from this initial pressure to the surface at a constant decompression rate. The model uses the alternating-direction implicit method to efficiently calculate the finite difference solution to the 3D anisotropic diffusion equation within the rectangular prism of olivine as its host magma undergoes syneruptive decompression. The diffusivities of water along the 'a', 'b', and 'c' crystallographic axes ( $D_a$ ,  $D_b$ , and  $D_c$ , respectively) are user-defined and assumed to be constant over the course of syneruptive magma ascent. We apply the temperature-dependent value of  $D_a$  determined by Barth et al. (2019b), and we assume that  $D_b = D_c$ . The goals of our 3D forward model calculations are as follows:

- (1) We aim to check the validity of the implicit assumption of our 1D Monte Carlo fitting procedure that the flux of water along the crystallographic 'b' and 'c' directions can be neglected.
- (2) We will assess the information content of water concentration gradients measured along the crystallographic 'c' axis; e.g., we will test whether  $D_a/D_c$  implied by our measured concentration gradients in natural olivine phenocrysts is consistent with experimental constraints on  $D_a/D_c$  (Ferriss et al., 2018; Barth et al., 2019b).

## 4. Results

### 4.1. Results of decompression rate modeling using olivine-hosted melt embayments at Segum volcano

As described in Section 3.5, we characterized concentration gradients of  $H_2O$ ,  $CO_2$ , S, Cl, and F in five olivine-hosted melt embayments from the 1977 eruption of Segum volcano. Of these five embayments, four exhibited concentration gradients in  $H_2O$ ,  $CO_2$ , and S produced during syneruptive ascent (see Fig. 4a, b, c and Supplementary information). We were unable to characterize the fifth embayment (EM3) sufficiently close to its outlet to resolve similar concentration gradients, so we omit that embayment from the following discussion. The four remaining embayments have concentration gradients in  $H_2O$ ,  $CO_2$ , and S that decrease monotonically towards vapor bubbles at their outlets, except for EM4, in which  $CO_2$  and S are observed to increase slightly in concentration towards the outlet while  $H_2O$  decreases. The monotonically decreasing volatile concentrations along the embayments are consistent with formation during syneruptive magma ascent and decompression, which led to diffusion-limited growth of the bubble at each embayment outlet. The observed increase in  $CO_2$  and S towards the outlet of EM4 may indicate a period of magma repressurization (Suckale et al., 2016) just prior to syneruptive decompression (i.e., the expected decrease in  $CO_2$  and S during syneruptive decompression may be confined to a region adjacent to the vapor bubble that was too narrow to be resolved by our nanoSIMS analyses), or alternatively, the magma hosting EM4 may have been fluxed with  $CO_2$  and S-rich vapor. For the purpose of this study, we have fit the volatile concentration gradients in four Segum embayments using the model described in Section 3.5 to constrain their syneruptive ascent histories. While we acknowledge that this simple decompression model does not capture every detail of the volatile concentration gradients in every embayment (particularly EM4), we focus here on deriving from the embayments important constraints on their syneruptive ascent histories. All data and model fits are provided in the Supplementary information and Supplementary data tables.

For each of the embayments, we used the model described in Section 3.5 to find the initial pressure ( $P_0$ ) and decompression rate ( $dP/dt$ ) that are best able to reproduce the measured volatile concentration gradients (Fig. 4). We find best-fit decompression rates that range from 0.02 to 0.13 MPa/s, with a mean of 0.07 MPa/s and a standard deviation of 0.05 MPa/s. The best-fit values of  $P_0$  range from 305 to 61 MPa. We observe a negative correlation between best-fit values of  $P_0$  and best-fit values of  $dP/dt$  (Fig. 4d): those embayments that appear to have stalled and/or crystallized deeper in the system prior to syneruptive ascent reflect slower average magma decompression rates and vice versa. We note that the simple one-stage linear decompression histories assumed by our model are likely an oversimplification: conduit models indicate that magma accelerates during ascent (Mastin and Ghiorso, 2000; Gonnermann and Manga, 2007), and a two-stage magma decompression model developed by Lloyd et al. (2014) found that  $CO_2$  and S gradients in melt embayments from the 1974 eruption of Fuego were better matched by



models that imposed a slow initial decompression rate followed by a more rapid second stage of decompression. The best-fit magma decompression rates constrained by our single-stage linear decompression model likely reflect the average decompression rates of the magma, so the observed negative correlation between initial pressure and decompression rate in Fig. 4 is exactly what we might expect for a magma that accelerates during ascent. Additionally, our observed S concentrations in the Segum embayments form plateaus at different S concentrations (Fig. 4a). Sulfur and water concentrations in olivine-, plagioclase- and pyroxene-hosted melt inclusions from Segum are positively correlated (Zimmer et al., 2010), indicating that sulfur and water degassed concurrently during this eruption, so plateaus in sulfur concentration observed along melt embayments from Segum suggest pre-eruptive stalling (for long enough to diffusively homogenize the sulfur concentration) and/or crystallization of the Segum magma at a range of depths.

#### 4.2. Results of decompression rate modeling using water concentration gradients in olivine phenocrysts

Every olivine that we analyzed is zoned in water (see Fig. 6, Supplementary information, and Supplementary data tables). In olivine phenocrysts that do not contain large melt inclusions, the zonation of water along the crystallographic 'a' direction can be used to constrain syn-eruptive magma decompression rates by applying the 1D Monte Carlo model described in Section 3.6. Applying this approach at Fuego, Segum, Kilauea Iki and Cerro Negro, we find best-fit decompression rates derived from our water-in-olivine model are in excellent agreement with decompression rates derived from modeling of volatile loss from melt embayments or melt inclusions (Fig. 7): All but one (CN95-ol9) of our  $dP/dt$  estimates from the water-in-olivine chronometer overlap (within two standard deviations) with the corresponding  $dP/dt$  estimates from melt embayments and melt inclusions. We note that the

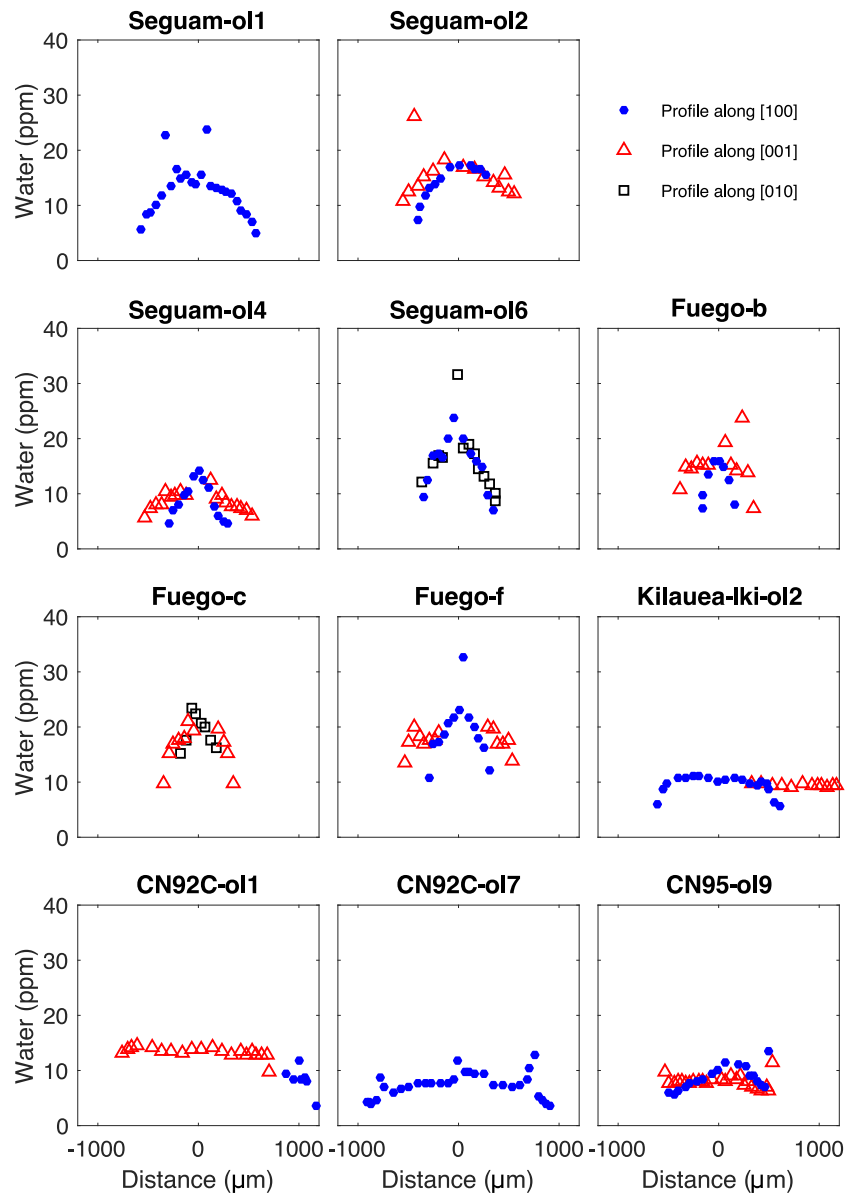


**Fig. 6.** Compilation of water concentration profiles measured in olivine phenocrysts from Segum, Fuego, Kilauea, and Cerro Negro volcanoes. Profiles measured along 'a' are plotted as filled blue circles, profiles measured along 'b' are plotted as open black squares, and profiles measured along 'c' are plotted as open red triangles. Distances are referenced to the centers of the phenocrysts. We note the presence of outliers along some of the profiles (e.g., two data points with >20 ppm H<sub>2</sub>O in Segum-ol1). These high-water outliers are typically associated with elevated concentrations of S, Cl, F and P, leading us to believe that they represent a contribution from tiny melt inclusions. Some high-water outliers are associated with elevated C, likely indicating surface contamination. All data are provided in the Supplementary data tables.

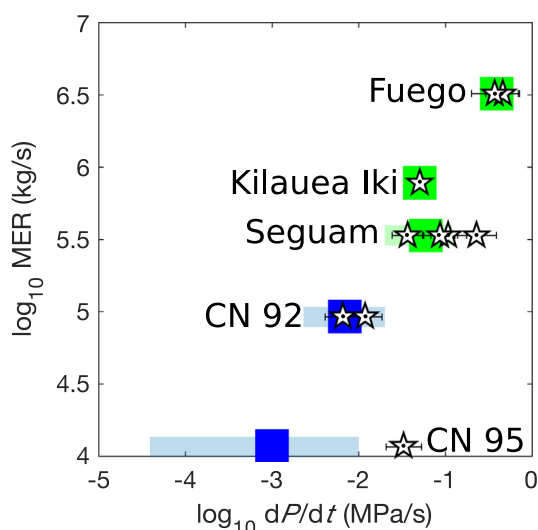


**Fig. 7.** Comparison of  $dP/dt$  values obtained using melt embayments (green squares) or water loss from olivine-hosted melt inclusions (blue squares) with best-fit  $dP/dt$  values obtained from our 1D Monte Carlo model of water diffusion in olivine phenocrysts (white stars), plotted against estimated mass extrusion rate (MER) for each studied eruption. Water-in-olivine data points are plotted at the mean of the 100 best-fit values determined by the Monte Carlo simulation; error bars on these points represent one standard deviation of these 100 best-fit values. The full range of  $dP/dt$  values derived from melt embayments and water loss from olivine-hosted melt inclusions are indicated by light-shaded color bars. Data sources for this figure are provided in Table 3.

water concentration profile measured across CN95-ol9 is asymmetric (Fig. 6), and the olivine phenocryst itself has an equant shape (i.e., the length of the crystal along ‘a’ is approximately equal to the length of the crystal along ‘c’, which is atypical compared to the majority of olivine phenocrysts from this eruption that have a long axis along ‘c’). These features of CN95-ol9 suggest that this phenocryst may have broken during ascent and/or may not be representative of the majority of olivine phenocrysts from this eruption. Phenocryst Fuego-c was not modeled because the polished plane through this phenocryst did not include the ‘a’ axis.

The differences in decompression rate experienced by the olivine phenocrysts presented in Fig. 6 can be intuited by considering the variations in phenocryst size and the concentrations of water measured in the centers of the phenocrysts. For example, phenocrysts from Fuego and Cerro Negro were hosted in magmas containing similar pre-eruptive water concentrations (Table 1), yet the relatively small phenocrysts erupted at Fuego contain higher central water concentrations on average than the relatively large phenocrysts from Cerro Negro (Fig. 6). The retention of higher water concentrations in the Fuego phenocrysts than the Cerro Negro phenocrysts suggests that the Fuego magma decompressed more rapidly than the Cerro Negro magma, thereby allowing less time for diffusive flux of water from the Fuego phenocrysts to the adjacent degassing melt.

**Table 3**  
Magma decompression rates using models of volatile loss from melt embayments (at Fuego, Seguam, and Kilauea Iki), olivine-hosted melt inclusions (at Cerro Negro) and the 1D Monte Carlo water-in-olivine chronometer. References: 1. Barth et al. (2019b); 2. Ferguson et al. (2016); and 3. Lloyd et al. (2014). Note that best-fit decompression rates for individual olivines (from all eruptions in this table) and embayments (from Seguam) are provided in the Supplementary data tables.

Eruption	$dP/dt$ (MPa/s) from embayments or MIs			Refs.	$dP/dt$ (MPa/s) from water in olivine			# phenocrysts
	Min	Max	Median		Min	Max	Median	
Cerro Negro 1992	2.3E–03	0.02	0.007	1 (MIs)	0.007	0.012	0.009	2
Cerro Negro 1995	3.89E–05	0.01	0.001	1 (MIs)	0.03	0.03	0.03	1
Seguam 1977	0.02	0.13	0.07	This study (emb)	0.04	0.23	0.10	4
Kilauea Iki 1959	0.045	0.055	0.05	2 (emb)	0.05	0.05	0.05	1
Fuego 1974	0.32	0.47	0.38	3 (emb)	0.38	0.45	0.41	2

Our best-fit decompression rates at Seguam span an order of magnitude (Table 3 and Supplementary data tables). The fact that this range is present in estimates from both the water-in-olivine chronometer and melt embayments supports the hypothesis that the measured range of  $dP/dt$  reflects real variability in magma decompression rate; however, some of this range may reflect artifacts in our dataset. For example, our water-in-olivine model does not take into account the presence of small melt inclusions in the olivine phenocrysts. Seguam-ol4 and Seguam-ol6 both contained small melt inclusions near their centers that were exposed at the polished surface. These inclusions likely acted as sources of water during syneruptive diffusive water loss from the phenocrysts, thereby ‘buffering’ water loss from the crystals and elevating their water concentrations to higher values than would be observed in an inclusion-free phenocryst that had experienced the same ascent history. By fitting water concentration gradients in melt-inclusion-bearing olivine phenocrysts with a model that does not account for the presence of melt inclusions, we expect a bias in our model results to high values of  $dP/dt$ . We expect the amount of bias introduced in our model to correlate with the size of the melt inclusions, the water concentration of the inclusions, and the proximity of the inclusions to the measured profile (Barth et al., 2019b). This expected bias in our results may explain the high best-fit  $dP/dt$  determined for Seguam-ol6, which contains a melt inclusion near its center.

## 5. Discussion

### 5.1. Advantages of the H-in-olivine magma ascent clock compared to existing methods

In Section 4.2, we demonstrate excellent agreement between magma decompression rates constrained by our 1D Monte Carlo water-in-olivine diffusion chronometer and magma decompression rates constrained by volatile diffusion along melt embayments or water loss from melt inclusions at eruptions of Fuego, Seguam, Kilauea and Cerro Negro. These techniques for constraining syneruptive magma decompression rates are largely independent of one another (e.g., the melt embayment model versus the water-in-olivine models use independently constrained diffusion coefficients and volatile solubility relationships), so agreement between the three techniques for the eruptions studied so far increases our confidence that our 1D water-in-olivine chronometer can provide robust estimates of magma decompression rates.

The prevalence of olivine phenocrysts in most basaltic to andesitic magma compositions means that water-in-olivine magma ascent chronometry can be applied to many volcanic systems. Furthermore, many olivine phenocrysts can be analyzed from a single eruption, such that it may be possible to resolve variations in magma decompression rates in both time (i.e., over the course of a single eruption or multiple eruptions) and space (i.e., variation in magma decompression rate recorded by phenocrysts erupted simultaneously at the same vent). This is a major advantage of the technique over existing methods for constraining magma decompression rates; e.g., olivine-hosted melt embayments tend to be rare (Lloyd et al., 2014; Ferguson et al., 2016).

## 5.2. Magma ascent at Kilauea Iki versus Segum and the importance of applying a degassing boundary condition

During magma ascent and decompression, the pressure at which magma begins to exsolve water vapor is dependent on the initial volatile content of the magma (Newman and Lowenstern, 2002). For example, magma erupted during the Kilauea Iki eruption containing ~0.78 wt% H<sub>2</sub>O (Ferguson et al., 2016) began to exsolve water vapor at a pressure of ~6 MPa (Newman and Lowenstern, 2002), while magma erupted at Segum volcano containing ~4.2 wt% water began to exsolve water vapor at a pressure of ~320 MPa (Fig. 8a and Table 2). We note that other parameters in addition to the initial water concentration of the magma (e.g., anhydrous magma composition and temperature; see Table 2) also influence the pressure at which the magma becomes saturated in water; these parameters are accounted for in Fig. 8a. Constraints on syneruptive magma decompression rates for the Kilauea Iki and Segum eruptions suggest that the Kilauea and Segum magmas decompressed at similar rates (Figs. 7, 8b), but the contrasting degassing histories of these magmas (Fig. 8a) result in surprisingly different records of diffusive water loss in their olivine phenocrysts:

our model suggests that olivine phenocrysts from Kilauea record diffusive water loss over a duration of ~3 min (Fig. 8c), whereas olivine phenocrysts from Segum record diffusive water loss over ~90 min (Fig. 8d). The comparison between records of diffusive water loss in olivine phenocrysts from Kilauea and Segum in Fig. 8 illustrates the sensitivity of our model to the degassing path assumed for the host magma.

We note that previous models of diffusive water loss from xenolith olivines during magma ascent have assumed a constant boundary condition of 0 wt% H<sub>2</sub>O (Demouchy et al., 2006; Peslier and Luhr, 2006; Thoraval and Demouchy, 2014; Peslier et al., 2015). In Fig. 9, we test the effect of assuming a constant boundary condition on the estimated magma decompression rate; our estimate of  $dP/dt$  for Segum-ol1 is an order of magnitude higher when we assume a constant boundary condition than if we apply a closed-system degassing boundary condition. The degassing boundary condition model also offers a modest improvement in goodness-of-fit to the data profile. This test underlines the sensitivity of the water-in-olivine magma ascent chronometer to the choice of boundary condition. We caution against the future use of models of syneruptive magma ascent that fail to account for the host magma degassing path.

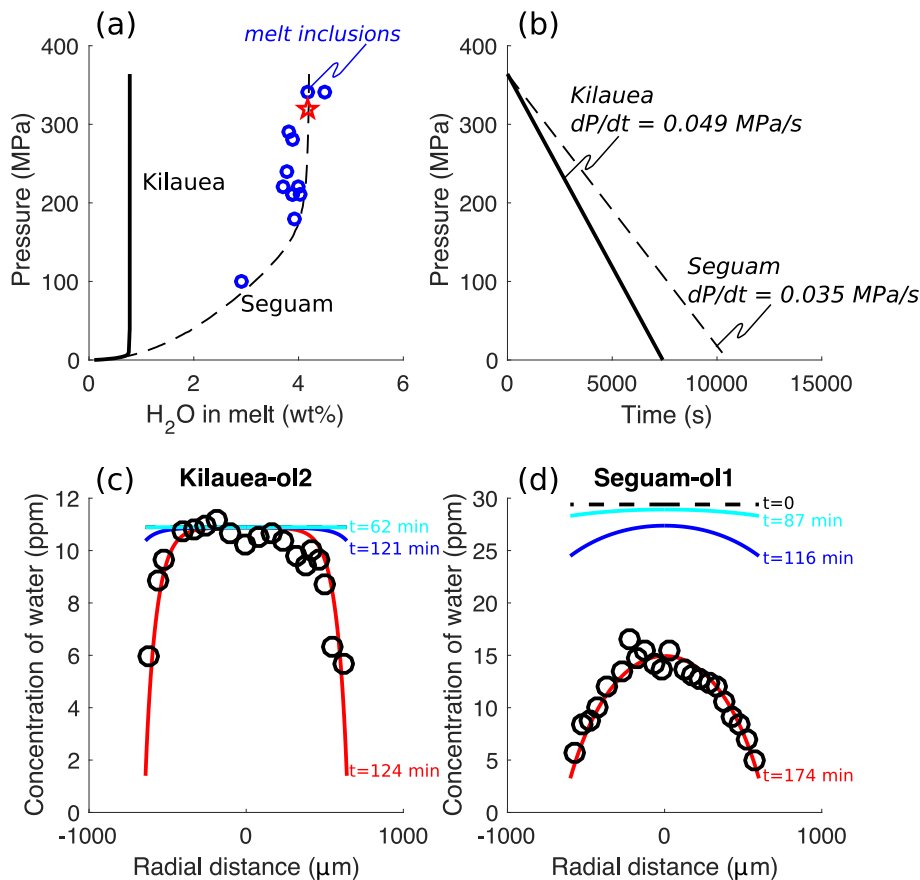


**Fig. 8.** Forward model of diffusive water loss from olivine phenocrysts at Kilauea Iki and Segum in response to syneruptive magma decompression and degassing. (a) Closed-system degassing paths of Segum magma (containing ~4.2 wt% water) and Kilauea magma (containing ~0.78 wt% water). The low water concentration of the Kilauea magma compared to a typical arc basalt allows the Kilauea magma to decompress to pressures of a few MPa before beginning to exsolve water. Conversely, Segum magma begins degassing water at a much higher pressure of ~320 MPa (indicated by the red star). Experimentally re-homogenized melt inclusions from Segum (blue circles; data from Moore et al., 2015) support the use of a closed-system degassing path at Segum and suggest that olivine crystallization occurs at pressures >~100 MPa (see discussion in Section 5.3). (b) Best-fit magma decompression histories for Segum (dashed line) and Kilauea (solid line) determined by the 1D Monte Carlo model suggest that these magmas decompressed at similar rates (see Fig. 7 and Table 3). (c) Comparison between calculated and measured water concentration gradients in olivine phenocryst Kilauea-Iki-ol2. Colored curves show modeled water concentration gradients after 62 min (cyan), 121 min (blue) and 124 min (red) of the 124-min decompression history. Note that the phenocryst remains unzoned for the first ~120 min of ascent because there is no water loss from the surrounding magma. (d) Comparison between calculated and measured water concentration gradients in olivine phenocryst Segum-ol1. Colored curves show modeled water concentration gradients after 87 min (cyan), 116 min (blue) and 174 min (red) of the 174-minute decompression history. The Segum olivine is hosted in a magma that continuously degasses water over ~320 MPa of decompression, so this phenocryst retains a long record of water loss over a period of ~100 min.

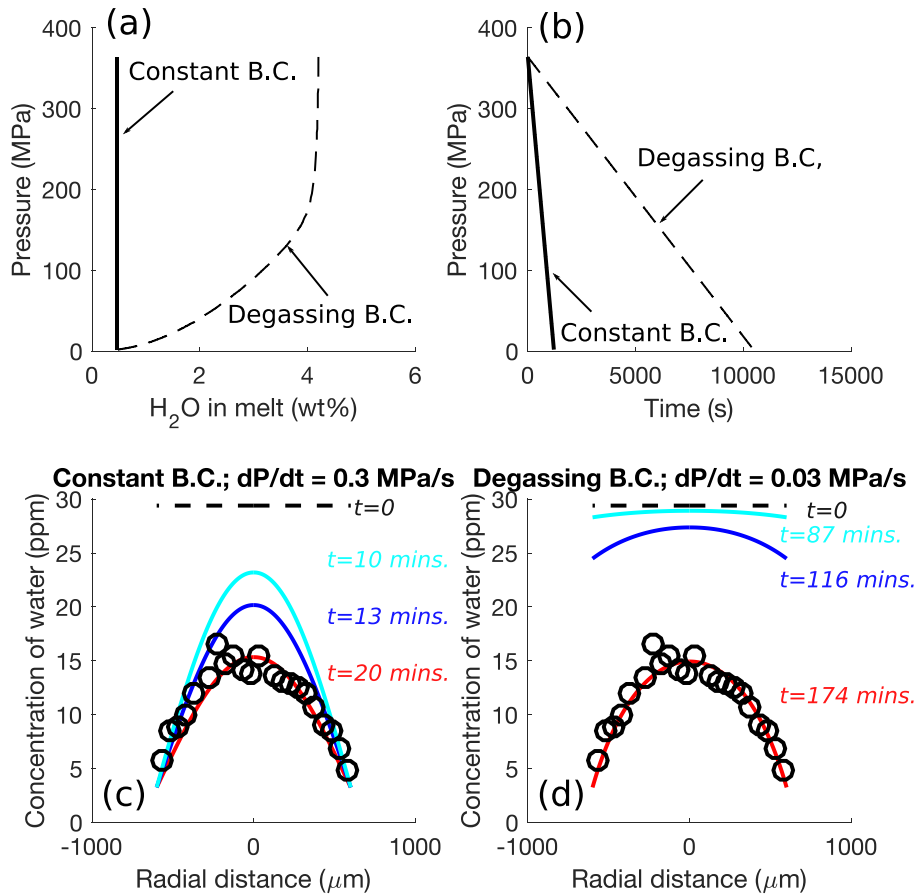


**Fig. 9.** Forward models of diffusive water loss from olivine phenocryst Segum-ol1 with constant and degassing boundary conditions. (a) Magma degassing paths assumed for the forward model. The dashed black line indicates a closed-system degassing boundary condition. The solid black line indicates a constant boundary condition; i.e., the water concentration of the host magma is assumed to contain ~0.5 wt% water throughout its ascent (chosen to approximately match the water content of the matrix glass at Segum). (b) Best-fit linear decompression histories found for Segum-ol1 with the constant and degassing boundary conditions imposed in (a). (c) Comparison between calculated and measured water concentration gradients in olivine phenocryst Segum-ol1, assuming a constant boundary condition and a decompression rate of 0.3 MPa/s. (d) Comparison between calculated and measured water concentration gradients in olivine phenocryst Segum-ol1, assuming a closed-system degassing boundary condition and a decompression rate of 0.03 MPa/s. Note that the application of a degassing boundary condition results in a best-fit decompression rate that is an order of magnitude lower than the best-fit decompression rate found using a constant boundary condition. The goodness-of-fit of the closed-system degassing model is also modestly better than that of the constant boundary condition model.

### 5.3. Depth sensitivity of the embayment chronometer vs. the water-in-olivine chronometer

An interesting feature of the Segum melt embayments presented in Section 4.1 is that they exhibit plateaus in their interior S concentrations that suggest stalling (for long enough to re-equilibrate their S concentrations along the lengths of the embayments) or crystallization at a range of depths prior to final ascent and eruption. Modeling of S and CO<sub>2</sub> in the Segum embayments is highly sensitive to initial pressure, and our best-fit initial pressures range from 61 to 305 MPa. In contrast to melt embayments, the water-in-olivine chronometer is insensitive to CO<sub>2</sub> and S degassing. The water-in-olivine chronometer begins recording magma decompression when water begins to exsolve from the host magma (~320 MPa at Segum; see Table 2 and Fig. 8a), because at pressures greater than the pressure of water saturation, the water dissolved in the olivine phenocrysts remains homogeneous and in equilibrium with the surrounding melt. For this reason, we selected the initial pressure for the water-in-olivine chronometer as the water saturation pressure. However, this choice does not account for the possibility that the olivines stalled or grew at pressures shallower than the water saturation pressure. There is evidence that arc magmas undergo degassing-driven crystallization over a range of pressures (Blundy and Cashman, 2005; Blundy et al., 2006). We can assess the pressure range of olivine crystallization using solubility models that relate measured

H<sub>2</sub>O and CO<sub>2</sub> concentrations in olivine-hosted melt inclusions to their entrapment pressures; e.g., Moore et al. (2015) find that the majority of Segum and Fuego olivine-hosted melt inclusions formed at pressures >~100 MPa (see Fig. 8a) and Barth et al. (2019b) find entrapment pressures for Cerro Negro olivine-hosted melt inclusions of >~96 MPa. Additionally, correlations between water and non-volatile incompatible oxides (e.g., K<sub>2</sub>O) can be used to assess the relationship between pressure and extent of crystallization (Roggensack, 2001). H<sub>2</sub>O and CO<sub>2</sub> concentrations in the least degassed olivine-hosted melt inclusions from Cerro Negro and Fuego are negatively correlated with K<sub>2</sub>O concentrations (Lloyd et al., 2013; Barth et al., 2019b). These negative correlations can be reproduced by degassing-driven crystallization models in which the magma crystallizes ~50% after the onset of water degassing. The pressure range of this crystallization is confined to depths >~96 MPa at Cerro Negro and >~100 MPa at Fuego (Lloyd et al., 2013; Barth et al., 2019b).

In order to test the error associated with our choice of initial pressure, we ran forward models with same decompression rate,  $K_d$ , and  $D_a$ , but different initial pressures (Fig. 10). We find that the model is remarkably insensitive to the choice of initial pressure, so this variable is unlikely to be a significant source of error in our best-fit values of  $dP/dt$ . This insensitivity of the decompression rate to the choice of initial pressure is a result of the fact that water solubility in the host melt closely approximates a square root function of pressure at the relatively



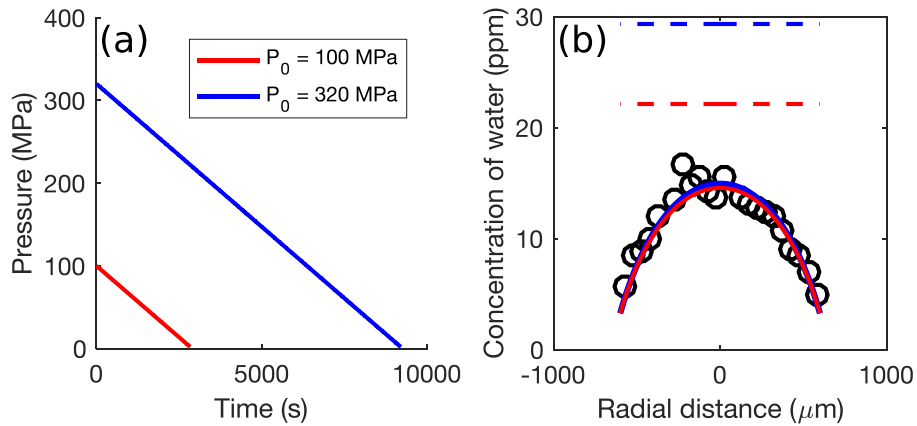


**Fig. 10.** Test of model sensitivity to the choice of initial pressure. (a) Imposed decompression histories for the forward model calculations. Both calculations assume a constant decompression rate of 0.03 MPa/s but different initial pressures (red line indicates  $P_0 = 100$  MPa; blue line indicates  $P_0 = 320$  MPa). (b) Forward model of diffusive water loss from olivine Segum-ol1 assuming the decompression histories plotted in (a). When  $P_0 = 320$  MPa, the initial water concentration in the olivine is fixed at ~30 ppm, but when  $P_0 = 100$  MPa the initial water concentration is reduced to ~22 ppm. The effect of the lower initial water concentration of the  $P_0 = 100$  MPa calculation is almost exactly counteracted by the shorter duration of decompression, such that the calculated water concentration gradient is insensitive to the choice of initial pressure, even for initial pressures that are lower than the pressure of water saturation (see discussion in Section 5.3).

low pressures considered by our model (Newcombe et al., 2017) such that the decrease in water concentration at the olivine-melt interface during decompression at a constant rate is proportional to the square root of time. The characteristic diffusion distance propagated by water in olivine during decompression is also a function of the square root of time; therefore, increasing the initial pressure of the model increases the initial water concentration in the olivine, but this increase is almost exactly compensated by the extra time available for diffusive water loss from a greater depth. Note that this trade-off between initial pressure and diffusive flux will be accurate only when the water diffusion front has reached the center of the phenocryst (i.e., when the characteristic diffusive lengthscale is equal to the length of the crystal).

#### 5.4. Testing the validity of the 1D model against a 3D model: when is the 1D approximation appropriate?

The 1D diffusion model described in Section 3.6 is easy to implement and fast to run compared with 3D models. However, 1D approximations to 3D systems must be applied with care in order to avoid the introduction of large systematic errors. In particular, our 1D model should only be applied to diffusion along the crystallographic 'a' axis [which can be identified using crystal morphology as in Fig. 2, by EBSD, by polarized Raman or FTIR spectroscopy (Asimow et al., 2006), etc.] in olivines containing as few inclusions of minerals or melts as possible.

In order to check the validity of the implicit assumption of our 1D Monte Carlo fitting procedure that the flux of water along the crystallographic 'b' and 'c' directions can be neglected, we ran 3D forward model calculations (using the model described in Section 3.6.2) in which we varied the  $D_a/D_c$  ratio; i.e., we varied the anisotropy of water diffusion in olivine from isotropic to strongly anisotropic. The results of these forward model calculations are shown in Fig. 11. The 3D forward model was set up to match the best-fit decompression histories found by the 1D model for Segum-ol2 and Fuego-b (these phenocrysts were selected because we measured their water concentration gradients along both 'a' and 'c'). The solid blue curves in Fig. 11 are calculated assuming  $D_c = 0$ , i.e., these curves in Fig. 11a and c are equivalent to curves calculated by the 1D model along 'a'. As  $D_c$  is increased to a value of  $D_a/40$ , there is no discernable change to the shape of the calculated water concentration gradient along 'a'. In order for water diffusion along 'c' to have a significant impact on the shape of the water concentration gradients along 'a', we find that  $D_c$  must be increased to values  $\geq D_a/3$ . The recent experimental study of Barth et al. (2019b) finds  $D_c \sim D_a/40$ , so this result appears to lend some confidence that the

implicit assumption of our 1D model that  $D_c = 0$  does not introduce significant error to our constraints of  $dP/dt$ . We note that our measurements of water concentration along 'a' and 'c' in Kilauea-Iki-ol2 are consistent with the diffusion anisotropy observed by Barth et al. (2019b): water concentration gradients measured along 'a' in this phenocryst propagate ~150  $\mu\text{m}$  towards the center of the crystal and we were unable to resolve a concentration gradient along 'c' in this crystal, implying a propagation distance of the dehydration profile along 'c' of  $< \sim 30$   $\mu\text{m}$  (i.e., the approximate spatial resolution of our SIMS analyses). The ratio of the estimated profile lengths along 'a' and 'c' in this crystal allow us to estimate  $D_c < \sim D_a/25$ .

Our measurements of water concentration gradients along 'c' in Segum-ol2 and Fuego-b also allow us to directly estimate the  $D_a/D_c$  ratio relevant to water loss from these natural olivine phenocrysts. The measured water concentration gradient along 'c' in Segum-ol2 propagates further towards the center of the phenocryst than would be expected for  $D_c \sim D_a/40$ . The shape of this gradient is instead more consistent with  $D_c \sim D_a/2$ . Similarly, the measured profile along 'c' in Fuego-b is also consistent with a higher value of  $D_a/D_c$  than expected from experimental observations (Barth et al., 2019b). The shapes of the concentration gradients along 'c' in Fig. 11b and d are seemingly inconsistent with the results of water diffusion experiments at 1000 °C and with the anisotropy of water concentration gradients observed in natural phenocryst Kilauea-Iki-ol2. Possible reasons for this apparent inconsistency include:

- (1) The profiles along 'c' may indicate that our Segum and Fuego phenocrysts ascended from greater depths and higher initial water concentrations than assumed by the models in Fig. 11. Note that the insensitivity of water concentration gradients along 'a' to initial pressure (Section 5.3) is applicable only to our 1D model for water loss along the fast 'a' direction. In contrast, the shapes of water concentration gradients along the slow 'b' and 'c' directions are likely to be highly sensitive to the initial pressure. Higher initial pressures at a fixed decompression rate would allow longer times for diffusive water loss along the slow 'b' and 'c' directions, which would produce concentration gradients along 'b' and 'c' that would propagate further towards the center of the phenocrysts.
- (2) The trace element chemistry of these phenocrysts may differ from the trace element chemistry of the natural olivine phenocrysts used in the experiments of Barth et al. (2019b), perhaps affecting  $K_d$  and/or the anisotropy of water diffusion (e.g., Hauri

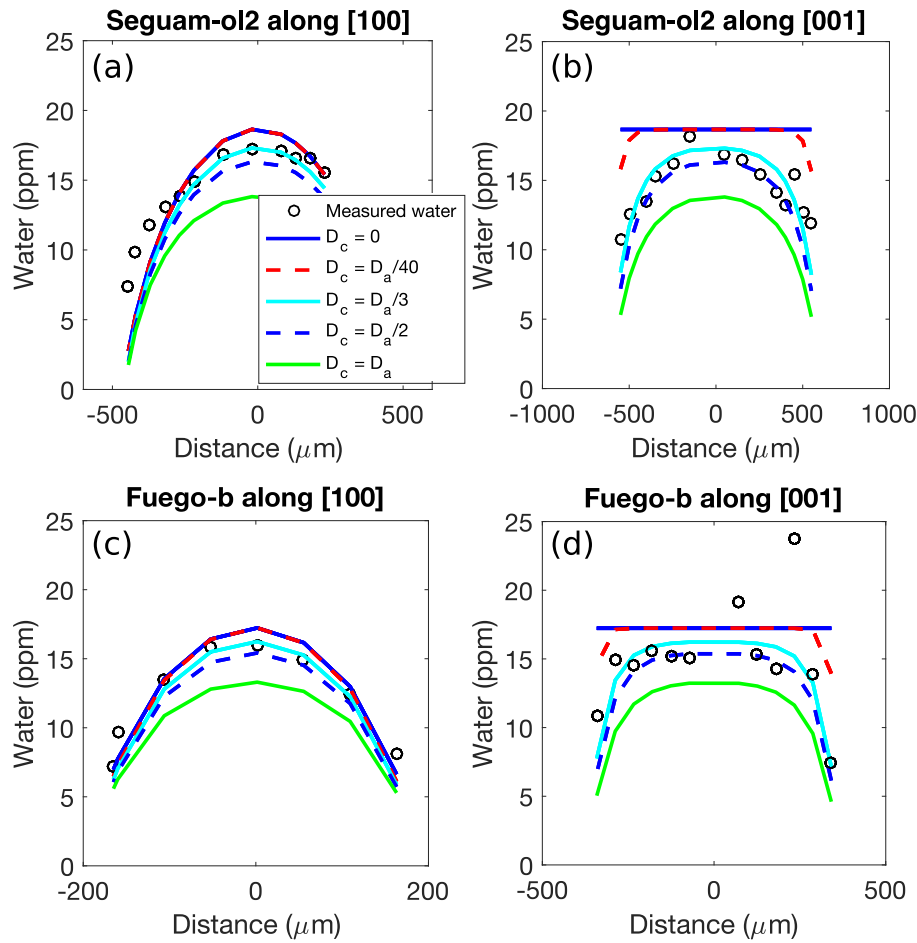


**Fig. 11.** 3D forward model calculations for Segum-ol2 and Fuego-b demonstrating the effect of changing the  $D_a/D_c$  ratio. (a) Model curves and measured data (black circles) along 'a' in Segum-ol2. Model calculations assume a closed-system degassing boundary condition, a constant  $dP/dt = 0.01$  MPa/s, and  $K_d = 0.0007$ . The diffusion anisotropy is varied from strongly anisotropic (i.e.,  $D_c = 0$ ; blue curve) to isotropic (i.e.,  $D_c = D_a$ ; green curve). (b) Model curves and measured data (black circles) along 'c' in Segum-ol2; model setup as in (a). Note that the diffusion front along 'c' reaches the center of the crystal for models in which  $D_c \geq D_a/3$ , thereby suggesting that, for this particular setup (crystal size, decompression history, temperature and degassing path), 1D approximations of water diffusion along 'a' will lose accuracy if  $D_c \geq D_a/3$ . (c) Model curves and measured data (black circles) along 'a' in Fuego-b. Model calculations assume a closed-system degassing boundary condition with a constant  $dP/dt = 0.36$  MPa/s and  $K_d = 0.0007$ . The diffusion anisotropy is varied as in the Segum-ol2 model. (d) Model curves and measured data (black circles) along 'c' in Fuego-b; model setup as in (c). See discussion in Section 5.4.

et al., 2006; Jollands et al., 2014).

- (3)  $D_a/D_c$  may vary with temperature (i.e., the activation energies of  $D_a$  and  $D_c$  may differ, see Fig. 3), thereby introducing inaccuracies in our extrapolation of the results of Barth et al. (2019b) to higher temperatures. However, we note that the extrapolation from 1000 °C to ~1070 °C for the Segum magma is relatively small, and it seems unlikely that there would be such a dramatic change in  $D_a/D_c$  over a temperature range of just 70 °C.
- (4) The decompression histories of the natural phenocrysts measured in this study are likely to be more complex than our simple model of one-stage linear decompression along a closed-system degassing path; e.g., the magma may convect in the conduit (Fowler and Robinson, 2018), the magma could be re-pressurized against a crystal-rich plug (Suckale et al., 2016; Barth et al., 2019a) and the magma degassing path could deviate from closed-system equilibrium behavior. Such complexities would have to be accounted for in our model in order to use water concentration gradients measured in natural phenocrysts to constrain  $D_a/D_c$ .
- (5) Our 3D model assumes a rectangular prism geometry for each olivine phenocryst; however, our natural olivine phenocrysts have a more complex geometry (Fig. 2). The rectangular prism geometry does not capture the thinning of the olivine towards the edges of the phenocrysts along 'a' and 'c', and the model may

therefore underestimate the propagation distance of water diffusion along 'a' and 'c'. We note that this issue does not affect the experiments of Barth et al. (2019b) or Ferriss et al. (2018), because their phenocrysts were polished into rectangular prisms prior to the dehydration experiments.

- (6) The water zonation observed along 'c' could be produced by growth of the Segum and Fuego phenocrysts during ascent in a progressively degassing magma. Melt inclusion data from Segum and Fuego suggest that olivine crystallization occurs over a pressure range of ~100–600 MPa (Moore et al., 2015). We show in Fig. 10 that this range of initial pressures has a negligible effect on the modeled water concentration gradients along 'a'; however, it is possible that syn-ascent growth in a progressively degassing magma could produce water zonation along the slow 'c' direction. The development of a 3D model of concurrent degassing, growth and diffusion would be required to test this hypothesis.

In summary, our 3D modeling suggests that diffusive flux of water along 'c' will have no discernable effect on the concentration gradient of water measured along 'a' for the decompression histories and crystal geometries considered in Fig. 11, if  $D_c < D_a/40$ . When  $D_c$  exceeds  $\sim D_a/3$ , the effect of diffusive flux of water along 'c' has a small but resolvable

effect on the water concentration gradient measured along 'a'. We assessed the magnitude of this effect by using our 1D Monte Carlo inversion technique to fit our 3D model-calculated water concentration gradient along 'a' in Seguam-ol2 with  $D_c = D_a / 2$ , and we recover a best-fit  $dP/dt$  that is a factor of 0.74 lower than the true  $dP/dt$ . Experimental constraints suggest that  $D_c < D_a / 40$ ; however, our measurements of water concentration gradients along 'c' in natural olivine phenocrysts from Fuego and Seguam propagate further towards the centers of the crystals than would be expected if  $D_c < D_a / 40$ . The experiments of Barth et al. (2019b) and Ferriss et al. (2018) were conducted on natural olivine phenocrysts with similar compositions to our Seguam and Fuego olivines, at similar temperatures, so it seems unlikely that differences in crystal chemistry or temperature could explain the high apparent  $D_c$  of Fuego-b and Seguam-ol2. Instead, we hypothesize that complexities in the decompression histories of these samples and the geometries and/or growth histories of the phenocrysts may be responsible for the unexpected shapes of water concentration gradients along 'c' in Fuego-b and Seguam-ol2. Experiments conducted over a wider range of temperatures and on a wider variety of olivine compositions will be required to better constrain the anisotropy of water diffusion in olivine and to better resolve when it will be necessary to use 3D modeling to accurately define decompression rates of olivines.

### 5.5. Summary of best practices for successful application of water-in-olivine magma ascent chronometry

In order to aid future applications of water-in-olivine magma ascent chronometry, we include here a summary of recommended methodologies for sample selection, analysis of water in olivine, and modeling of water concentration data.

- (1) *Sample selection:* Water-in-olivine magma ascent chronometry is most easily applied to olivine phenocrysts that are euhedral (such that they can be oriented based on their morphology) and coated in vesicular glass (thereby demonstrating their direct contact with degassing magma during ascent). 1D modeling is best applied along the crystallographic 'a' axis in phenocrysts that do not contain melt inclusions. The sensitivity of the technique to low magma decompression rates is dependent on crystal size: water concentration gradients are more rapidly erased from small phenocrysts than large phenocrysts, so large phenocrysts should be selected for analysis where possible.
- (2) *Analysis of water concentration gradients in olivine:* Water concentration gradients can be characterized in olivine phenocrysts using SIMS or FTIR. FTIR offers the advantages that it is relatively inexpensive, analyses are fast (maps of entire crystals can be produced in ~1 h), and FTIR spectra contain information about sites in the olivine structure in which protons are bonded. The main disadvantage of FTIR is that analyses in three perpendicular directions are required in order to determine absolute values of bulk water concentration. The small sizes and complex geometries of most olivine phenocrysts make this difficult to achieve. SIMS offers the advantage of higher spatial resolution than FTIR, although it is a more expensive and less accessible technique. A potentially fruitful avenue for future studies may be a combined FTIR and SIMS approach, in which the shapes of water concentration gradients are mapped by FTIR, and absolute water concentrations are determined in the centers and edges of the phenocrysts by SIMS.
- (3) *Model setup for determining magma decompression rates:* Application of water-in-olivine magma ascent chronometry requires prior knowledge of the initial water concentration of the magma and an estimation of the degassing path of the magma during decompression. The initial water concentration of the magma is typically assumed to correspond to the highest measured water concentration in olivine-hosted melt inclusions

(Plank et al., 2013; Moore et al., 2015) and open- or closed-system degassing paths can be calculated for the magma using published volatile solubility models such as VolatileCalc (Newman and Lowenstern, 2002). The 1D modeling approach developed in this study is easy to implement but its accuracy may be compromised by the presence of melt and/or mineral inclusions in the olivine phenocrysts. For this reason, we recommend the selection of olivine phenocrysts without melt inclusions. Future developments of 3D modeling techniques in which complex crystal geometries and the presence of melt inclusions can be accounted for may increase the accuracy and applicability of water-in-olivine magma decompression chronometry. Indeed, the concentration of water in olivine-hosted melt inclusions provides an additional constraint of magma decompression rate (Chen et al., 2011; Barth et al., 2019b), and the application of water-in-olivine magma decompression chronometry to inclusion-bearing phenocrysts could be a powerful approach.

## 6. Conclusions

Recent experimental work has provided important constraints on the behavior of water in olivine during syneruptive degassing-driven diffusion (Ferriss et al., 2018; Barth et al., 2019b). We have applied these findings to develop a new magma ascent chronometer that uses concentration gradients of water along the fast 'a' direction in natural olivine phenocrysts to constrain syneruptive magma decompression rates. We use a Monte Carlo approach to assess the effects of uncertainties in our input parameters (e.g., temperature and  $K_d$ ) on the decompression rates derived by our model. We have also performed sensitivity tests to assess the impact on our derived decompression rates of the choice of initial pressure (Section 5.3) and the assumption of our 1D model that the flux of water along the 'b' and 'c' directions can be neglected (Section 5.4). Under the conditions tested, best-fit  $dP/dt$  values are found to be robust over a large range of initial pressures, and we find that the assumption of zero water flux along 'b' and 'c' is unlikely to be a major source of error.

We have tested our model on eruptions for which constraints of syneruptive magma decompression rate already exist, either from models of volatile diffusion along melt embayments (Lloyd et al., 2014; Ferguson et al., 2016) or from models of diffusive water loss from olivine-hosted melt inclusions (Barth et al., 2019b). We find excellent agreement between  $dP/dt$  values constrained by our water-in-olivine chronometer and estimated by these existing techniques for all but one of the phenocrysts studied (Fig. 7). This test confirms the accuracy and sensitivity of the water-in-olivine chronometer over a range of  $dP/dt$  values spanning ~2 orders of magnitude.

Our results reveal a wide range of best-fit values of  $dP/dt$  at Seguam. This range is evident both in water-in-olivine chronometer estimates and in diffusive volatile loss from melt embayment estimates (Fig. 7). Additionally, plateaus of S concentration observed in melt embayments from Seguam suggest pre-eruptive stalling or crystallization of the Seguam magma at a range of depths, and we find higher  $dP/dt$  values in the melt embayments that appear to have stalled or crystallized at the shallowest depths (Fig. 4).

A major strength of the water-in-olivine chronometer is the prevalence of olivine in mafic to intermediate magmas. Every olivine we analyzed was strongly zoned along the fast 'a' direction, so we expect that this new technique will allow the compilation of many values of  $dP/dt$  from single eruptions. This may open a path to studying changes in  $dP/dt$  through time and space, which will provide a more detailed window into syneruptive conduit processes than has been possible using other techniques for constraining  $dP/dt$ . We note that the majority of olivines we analyzed also showed zonation along 'b' and 'c' (Fig. 6) and

this zonation may provide additional constraints on magma decompression histories via a 3D modeling approach (Fig. 11).

This study has highlighted the need for further experimental work to constrain the partitioning and diffusion behavior of water at the low pressures relevant to ascent through the shallow crust. Another important avenue for future research will be the application of fast mapping techniques for measuring water concentration gradients in olivine phenocrysts (e.g., FTIR). Such techniques could in theory pave the way for 'rapid response petrology'; e.g., the constraint of magma decompression rates could be performed during an active eruption to inform models of conduit processes and volcanic hazard.

### CRediT authorship contribution statement

**Megan E. Newcombe:** Conceptualization, Investigation, Methodology, Software, Writing - original draft, Writing - review & editing, Funding acquisition. **Terry Plank:** Conceptualization, Writing - original draft, Writing - review & editing, Resources, Supervision. **Anna Barth:** Investigation, Writing - original draft, Writing - review & editing. **Paul D. Asimow:** Software, Validation, Writing - original draft, Writing - review & editing. **Erik Hauri:** Resources, Methodology, Investigation.

### Declaration of competing interest

The authors declare that they have no known competing financial interests or personal relationships that could have appeared to influence the work reported in this paper.

### Acknowledgements

This paper is dedicated to Erik Hauri, a greatly missed mentor and friend. We are grateful to Jianhua Wang, Adrian Fiege, David Ferguson, and Michael Guerette for their help with the nanoSIMS, electron microprobe, and electron backscatter diffraction analyses. Alexander Lloyd is thanked for preparing and analyzing the Segum embayments, and Alexander Lloyd and Elizabeth Ferriss are thanked for insightful discussions. We are grateful for constructive and valuable reviews by Madison Myers and an anonymous reviewer. Newcombe acknowledges support from NSF GeoPRISMS grant #1551868.

### Appendix A. Supplementary data

Supplementary data to this article can be found online at <https://doi.org/10.1016/j.jvolgeores.2020.106872>.

### References

- Adam, J., Turner, M., Hauri, E.H., Turner, S., 2016. Crystal/melt partitioning of water and other volatiles during the near-solidus melting of mantle peridotite: comparisons with non-volatile incompatible elements and implications for the generation of intraplate magmatism. *Am. Mineral.* 101 (4), 876–888. <https://doi.org/10.2138/am-2016-5437>.
- Asimow, P.D., Stein, L.C., Mosenfelder, J.L., Rossman, G.R., 2006. Quantitative polarized infrared analysis of trace OH in populations of randomly oriented mineral grains. *Am. Mineral.* 91 (2–3), 278–284.
- Aubaud, C., Hauri, E.H., Hirschmann, M.M., 2004. Hydrogen partition coefficients between nominally anhydrous minerals and basaltic melts. *Geophys. Res. Lett.* 31 (20). <https://doi.org/10.1029/2004GL021341>.
- Barth, A., Edmonds, M., Woods, A., 2019a. Valve-like dynamics of gas flow through a packed crystal mush and cyclic strombolian explosions. *Sci. Rep.* 9 (1), 821.
- Barth, A., Newcombe, M., Plank, T., Gonnermann, H., Hajimirza, S., Soto, G.J., Saballos, A., Hauri, E., 2019b. Control of magma decompression rate on explosivity at basaltic-intermediate volcanoes — constraints from water diffusion in olivine. *J. Volcanol. Geotherm. Res.* 387.
- Bell, D.R., Rossman, G.R., 1992. Water in earth's mantle - the role of nominally anhydrous minerals. *Science* 255 (5050), 1391–1397.
- Bell, D.R., Rossman, G.R., Maldener, J., Endisch, D., Rauch, F., 2003. Hydroxide in olivine: a quantitative determination of the absolute amount and calibration of the IR spectrum. *J. Geophys. Res. Solid Earth* 108 (B2). <https://doi.org/10.1029/2001jb000679> n/a-n/a.
- Berlo, K., Blundy, J., Turner, S., Cashman, K., Hawkesworth, C., Black, S., 2004. Geochemical precursors to volcanic activity at Mount St. Helens, USA. *Science* 306 (5699), 1167–1169.
- Berlo, K., Stix, J., Roggensack, K., Ghaleb, B., 2012. A tale of two magmas, Fuego, Guatemala. *Bull. Volcanol.* 74 (2), 377–390. <https://doi.org/10.1007/s00445-011-0530-8>.
- Blundy, J., Cashman, K., 2005. Rapid decompression-driven crystallization recorded by melt inclusions from Mount St. Helens volcano. *Geology* 33 (10), 793–796. <https://doi.org/10.1130/g21668.1>.
- Blundy, J., Cashman, K., Humphreys, M., 2006. Magma heating by decompression-driven crystallization beneath andesite volcanoes. *Nature* 443 (7107), 76.
- Blundy, J., Cashman, K.V., Rust, A., Witham, F., 2010. A case for CO<sub>2</sub>-rich arc magmas. *Earth Planet. Sci. Lett.* 290 (3), 289–301. <https://doi.org/10.1016/j.epsl.2009.12.013>.
- Caricchi, L., Sheldrake, T.E., Blundy, J., 2018. Modulation of magmatic processes by CO<sub>2</sub> flushing. *Earth Planet. Sci. Lett.* 491, 160–171. <https://doi.org/10.1016/j.epsl.2018.03.042>.
- Cassidy, M., Manga, M., Cashman, K., Bachmann, O., 2018. Controls on explosive-effusive volcanic eruption styles. *Nat. Commun.* 9 (1), 2839.
- Chen, Y., Provost, A., Schiano, P., Cluzel, N., 2011. The rate of water loss from olivine-hosted melt inclusions. *Contrib. Mineral. Petrol.* 162 (3), 625–636. <https://doi.org/10.1007/s00410-011-0616-5>.
- Chen, Y., Provost, A., Schiano, P., Cluzel, N., 2013. Magma ascent rate and initial water concentration inferred from diffusive water loss from olivine-hosted melt inclusions. *Contrib. Mineral. Petrol.* 165 (3), 525–541. <https://doi.org/10.1007/s00410-012-0821-x>.
- Demouchy, S., Mackwell, S., 2006. Mechanisms of hydrogen incorporation and diffusion in iron-bearing olivine. *Phys. Chem. Miner.* 33 (5), 347–355. <https://doi.org/10.1007/s00269-006-0081-2>.
- Demouchy, S., Jacobsen, S.D., Gaillard, F., Stern, C.R., 2006. Rapid magma ascent recorded by water diffusion profiles in mantle olivine. *Geology* 34 (6), 429–432. <https://doi.org/10.1130/g22386.1>.
- Eaton, J.P., Richter, D.H., Krivoy, H.L., 1987. Cycling of magma between the summit reservoir and Kilauea Iki lava lake during the 1959 eruption of Kilauea volcano. *US Geol. Surv. Prof. Pap.* 1350, 1307–1335.
- Edmonds, M., 2008. New geochemical insights into volcanic degassing. *Philos. Trans. R. Soc. A Math. Phys. Eng. Sci.* 366 (1885), 4559–4579. <https://doi.org/10.1098/rsta.2008.0185>.
- Ferguson, D.J., Gonnermann, H.M., Ruprecht, P., Plank, T., Hauri, E.H., Houghton, B.F., Swanson, D.A., 2016. Magma decompression rates during explosive eruptions of Kilauea volcano, Hawaii, recorded by melt embayments. *Bull. Volcanol.* 78 (10), 71. <https://doi.org/10.1007/s00445-016-1064-x>.
- Ferriss, E., Plank, T., Newcombe, M., Walker, D., Hauri, E., 2018. Rates of dehydration of olivines from San Carlos and Kilauea Iki. *Geochim. Cosmochim. Acta* 242, 165–190.
- Fowler, A.C., Robinson, M., 2018. Counter-current convection in a volcanic conduit. *J. Volcanol. Geotherm. Res.* 356, 141–162. <https://doi.org/10.1016/j.jvolgeores.2018.03.004>.
- Gonnermann, H.M., Manga, M., 2007. The fluid mechanics inside a volcano. *Annu. Rev. Fluid Mech.* 39 (1), 321–356. <https://doi.org/10.1146/annurev.fluid.39.050905.110207>.
- Hauri, E., 2002. SIMS analysis of volatiles in silicate glasses, 2: isotopes and abundances in Hawaiian melt inclusions. *Chem. Geol.* 183 (1–4), 115–141. [https://doi.org/10.1016/S0009-2541\(01\)00374-6](https://doi.org/10.1016/S0009-2541(01)00374-6).
- Hauri, E., Wang, J., Dixon, J.E., King, P.L., Mandeville, C., Newman, S., 2002. SIMS analysis of volatiles in silicate glasses: 1. Calibration, matrix effects and comparisons with FTIR. *Chem. Geol.* 183 (1–4), 99–114. [https://doi.org/10.1016/S0009-2541\(01\)00375-8](https://doi.org/10.1016/S0009-2541(01)00375-8).
- Hauri, E.H., Gaetani, G.A., Green, T.H., 2006. Partitioning of water during melting of the Earth's upper mantle at H<sub>2</sub>O-undersaturated conditions. *Earth Planet. Sci. Lett.* 248 (3–4), 715–734. <https://doi.org/10.1016/j.epsl.2006.06.014>.
- Hauri, E.H., Weinreich, T., Saal, A.E., Rutherford, M.C., Van Orman, J.A., 2011. High pre-eruptive water contents preserved in lunar melt inclusions. *Science* 333 (6039), 213–215. <https://doi.org/10.1126/science.1204626>.
- Hill, B.E., Connor, C.B., Jarzempa, M.S., La Femina, P.C., Navarro, M., Strauch, W., 1998. 1995 eruptions of Cerro Negro volcano, Nicaragua, and risk assessment for future eruptions. *Geol. Soc. Am. Bull.* 110 (10), 1231–1241.
- Huber, C., Su, Y., Nguyen, C.T., Parmigiani, A., Gonnermann, H.M., Dufek, J., 2014. A new bubble dynamics model to study bubble growth, deformation, and coalescence. *J. Geophys. Res. Solid Earth* 119 (1), 216–239. <https://doi.org/10.1002/2013JB010419>.
- Humphreys, M.C., Menand, T., Blundy, J.D., Klimm, K., 2008. Magma ascent rates in explosive eruptions: constraints from H<sub>2</sub>O diffusion in melt inclusions. *Earth Planet. Sci. Lett.* 270 (1–2), 25–40.
- Jicha, B.R., Singer, B.S., 2006. Volcanic history and magmatic evolution of Segum Island, Aleutian Island arc, Alaska. *Geol. Soc. Am. Bull.* 118 (7–8), 805–822. <https://doi.org/10.1130/b25861.1>.
- Jollands, M.C., O'Neill, H.S.C., Hermann, J., 2014. The importance of defining chemical potentials, substitution mechanisms and solubility in trace element diffusion studies: the case of Zr and Hf in olivine. *Contrib. Mineral. Petrol.* 168 (3), 1055.
- Koga, K., Hauri, E., Hirschmann, M., Bell, D., 2003. Hydrogen concentration analyses using SIMS and FTIR: comparison and calibration for nominally anhydrous minerals. *Geochim. Geophys. Res.* 4 (2). <https://doi.org/10.1029/2002GC000378> n/a-n/a.
- Kohlstedt, D.L., Mackwell, S.J., 1998. Diffusion of hydrogen and intrinsic point defects in olivine. *Z. Phys. Chem.* 207. [https://doi.org/10.1524/zpch.1998.207.Part\\_1\\_2.147](https://doi.org/10.1524/zpch.1998.207.Part_1_2.147).
- Kumamoto, K.M., Warren, J.M., Hauri, E.H., 2017. New SIMS reference materials for measuring water in upper mantle minerals. *Am. Mineral.* 102 (3), 537–547.
- La Spina, G., Burton, M., de' Michieli Vitturi, M., 2015. Temperature evolution during magma ascent in basaltic effusive eruptions: a numerical application to Stromboli



- volcano. *Earth Planet. Sci. Lett.* 426, 89–100. <https://doi.org/10.1016/j.epsl.2015.06.015>.
- Le Voyer, M., Asimow, P.D., Mosenfelder, J.L., Guan, Y., Wallace, P.J., Schiano, P., Stolper, E.M., Eiler, J.M., 2014. Zonation of H<sub>2</sub>O and F concentrations around melt inclusions in olivines. *J. Petrol.* <https://doi.org/10.1093/ptrology/egu003>.
- Llewellyn, E.W., Manga, M., 2005. Bubble suspension rheology and implications for conduit flow. *J. Volcanol. Geotherm. Res.* 143 (1), 205–217. <https://doi.org/10.1016/j.jvolgeores.2004.09.018>.
- Lloyd, A., Plank, T., Ruprecht, P., Hauri, E., Rose, W., 2013. Volatile loss from melt inclusions in pyroclasts of differing sizes. *Contrib. Mineral. Petrol.* 165 (1), 129–153. <https://doi.org/10.1007/s00410-012-0800-2>.
- Lloyd, A.S., Ruprecht, P., Hauri, E.H., Rose, W., Gonnermann, H.M., Plank, T., 2014. NanoSIMS results from olivine-hosted melt embayments: magma ascent rate during explosive basaltic eruptions. *J. Volcanol. Geotherm. Res.* 283, 1–18. <https://doi.org/10.1016/j.jvolgeores.2014.06.002>.
- Lloyd, A.S., Ferriss, E., Ruprecht, P., Hauri, E.H., Jicha, B.R., Plank, T., 2016. An assessment of clinopyroxene as a recorder of magmatic water and magma ascent rate. *J. Petrol.* 57 (10), 1865–1886. <https://doi.org/10.1093/ptrology/egw058>.
- Long, G.L., Winefordner, J.D., 1983. Limit of detection a closer look at the IUPAC definition. *Anal. Chem.* 55 (7), 712A–724A. <https://doi.org/10.1021/ac00258a724>.
- Mastin, L.G., Ghiorso, M.S., 2000. *A Numerical Program for Steady-state Flow of Magma-Gas Mixtures Through Vertical Eruptive Conduits*. Department of the Interior, Washington DC.
- McClelland, L., 1992. Global Volcanism Program; report on Cerro Negro (Nicaragua). Bulletin of the Global Volcanism Network. 17. Smithsonian Institution, p. 4. <https://doi.org/10.5479/si.GVP.BGVN199204-344070>.
- Médard, E., Grove, T.L., 2008. The effect of H<sub>2</sub>O on the olivine liquidus of basaltic melts: experiments and thermodynamic models. *Contrib. Mineral. Petrol.* 155 (4), 417–432. <https://doi.org/10.1007/s00410-007-0250-4>.
- Miller, T.P., McGimsey, R., Richter, D., Riehle, J., Nye, C., Yount, M., Dumoulin, J., 1998. Catalog of the Historically Active Volcanoes of Alaska. Citeseer.
- Moore, L.R., Gazel, E., Tuohy, R., Lloyd, A.S., Esposito, R., Steele-MacInnis, M., Hauri, E.H., Wallace, P.J., Plank, T., Bodnar, R.J., 2015. Bubbles matter: an assessment of the contribution of vapor bubbles to melt inclusion volatile budgets. *Am. Mineral.* 100 (4), 806–823. <https://doi.org/10.2138/am-2015-5036>.
- Mosenfelder, J.L., Le Voyer, M., Rossman, G.R., Guan, Y., Bell, D.R., Asimow, P.D., Eiler, J.M., 2011. Analysis of hydrogen in olivine by SIMS: evaluation of standards and protocol. *Am. Mineral.* 96 (11–12), 1725–1741. <https://doi.org/10.2138/am.2011.3810>.
- Myers, M.L., Wallace, P.J., Wilson, C.J.N., Morter, B.K., Swallow, E.J., 2016. Prolonged ascent and episodic venting of discrete magma batches at the onset of the Huckleberry Ridge supereruption, Yellowstone. *Earth Planet. Sci. Lett.* 451, 285–297. <https://doi.org/10.1016/j.epsl.2016.07.023>.
- Myers, M.L., Wallace, P.J., Wilson, C.J., Watkins, J.M., Liu, Y., 2018. Ascent Rates of Rhyolitic Magma at the Onset of Three Caldera-forming Eruptions. *Mineralogical Society of America*.
- Newcombe, M., Brett, A., Beckett, J., Baker, M., Newman, S., Guan, Y., Eiler, J., Stolper, E., 2017. Solubility of water in lunar basalt at low pH<sub>2</sub>O. *Geochim. Cosmochim. Acta* 200, 330–352.
- Newman, S., Lowenstern, J.B., 2002. VolatileCalc: a silicate melt–H<sub>2</sub>O–CO<sub>2</sub> solution model written in Visual Basic for excel. *Comput. Geosci.* 28 (5), 597–604. [https://doi.org/10.1016/S0098-3004\(01\)00081-4](https://doi.org/10.1016/S0098-3004(01)00081-4).
- Ni, H., Zhang, L., 2018. A general model of water diffusivity in calc-alkaline silicate melts and glasses. *Chem. Geol.* 478, 60–68. <https://doi.org/10.1016/j.chemgeo.2017.10.010>.
- Peslier, A.H., Luhr, J.F., 2006. Hydrogen loss from olivines in mantle xenoliths from Simcoe (USA) and Mexico: mafic alkaline magma ascent rates and water budget of the sub-continental lithosphere. *Earth Planet. Sci. Lett.* 242 (3), 302–319.
- Peslier, A.H., Bizimis, M., Matney, M., 2015. Water disequilibrium in olivines from Hawaiian peridotites: recent metasomatism, H diffusion and magma ascent rates. *Geochim. Cosmochim. Acta* 154, 98–117.
- Plank, T., Kelley, K.A., Zimmer, M.M., Hauri, E.H., Wallace, P.J., 2013. Why do mafic arc magmas contain ~4 wt% water on average? *Earth Planet. Sci. Lett.* 364, 168–179.
- Proussevitch, A., Sahagian, D., 2005. Bubbledrive-1: a numerical model of volcanic eruption mechanisms driven by disequilibrium magma degassing. *J. Volcanol. Geotherm. Res.* 143 (1), 89–111. <https://doi.org/10.1016/j.jvolgeores.2004.09.012>.
- Richter, D.H., Eaton, J.P., Murata, K.J., Ault, W.U., Krivoy, H.L., 1970. Chronological Narrative of the 1959–60 Eruption of Kilauea Volcano, Hawaii (Professional Paper, - edn).
- Roggensack, K., 2001. Unraveling the 1974 eruption of Fuego volcano (Guatemala) with small crystals and their young melt inclusions. *Geology* 29 (10), 911–914. [https://doi.org/10.1130/0091-7613\(2001\)029<0911:uteofv>2.0.co;2](https://doi.org/10.1130/0091-7613(2001)029<0911:uteofv>2.0.co;2).
- Rose, W.I., Anderson, A.T., Woodruff, L.G., Bonis, S.B., 1978. The October 1974 basaltic tephra from Fuego volcano: description and history of the magma body. *J. Volcanol. Geotherm. Res.* 4 (1), 3–53. [https://doi.org/10.1016/0377-0273\(78\)90027-6](https://doi.org/10.1016/0377-0273(78)90027-6).
- Rose, W.I., Self, S., Murrow, P.J., Bonadonna, C., Durant, A.J., Ernst, G.G.J., 2008. Nature and significance of small volume fall deposits at composite volcanoes: insights from the October 14, 1974 Fuego eruption, Guatemala. *Bull. Volcanol.* 70 (9), 1043–1067. <https://doi.org/10.1007/s00445-007-0187-5>.
- Rutherford, M.J., Devine, J.D., 2003. Magmatic conditions and magma ascent as indicated by hornblende phase equilibria and reactions in the 1995–2002 Soufrière Hills magma. *J. Petrol.* 44 (8), 1433–1453. <https://doi.org/10.1093/ptrology/44.8.1433>.
- Shea, T., Costa, F., Krimer, D., Hammer, J.E., 2015. Accuracy of timescales retrieved from diffusion modeling in olivine: a 3D perspective. *Am. Mineral.* 100 (10), 2026–2042.
- Sides, I., Edmonds, M., MacLennan, J., Houghton, B., Swanson, D., Steele-MacInnis, M., 2014. Magma mixing and high fountaining during the 1959 Kilauea Iki eruption, Hawaii. *Earth Planet. Sci. Lett.* 400, 102–112.
- Sisson, T.W., Layne, G.D., 1993. H<sub>2</sub>O in basalt and basaltic andesite glass inclusions from four subduction-related volcanoes. *Earth Planet. Sci. Lett.* 117 (3), 619–635. [https://doi.org/10.1016/0012-821X\(93\)90107-K](https://doi.org/10.1016/0012-821X(93)90107-K).
- Sparks, R.S.J., 1978. The dynamics of bubble formation and growth in magmas: a review and analysis. *J. Volcanol. Geotherm. Res.* 3 (1), 1–37. [https://doi.org/10.1016/0377-0273\(78\)90002-1](https://doi.org/10.1016/0377-0273(78)90002-1).
- Stovall, W.K., Houghton, B.F., Gonnermann, H., Fagents, S.A., Swanson, D.A., 2011. Eruption dynamics of Hawaiian-style fountains: the case study of episode 1 of the Kilauea Iki 1959 eruption. *Bull. Volcanol.* 73 (5), 511–529. <https://doi.org/10.1007/s00445-010-0426-z>.
- Suckale, J., Hager, B.H., Elkins-Tanton, L.T., Nave, J.C., 2010. It takes three to tango: 2. Bubble dynamics in basaltic volcanoes and ramifications for modeling normal Strombolian activity. *J. Geophys. Res. Solid Earth* 115 (B7). <https://doi.org/10.1029/2009JB006917>.
- Suckale, J., Keller, T., Cashman, K., Persson, P.O., 2016. Flow-to-fracture transition in a volcanic mush plug may govern normal eruptions at Stromboli. *Geophys. Res. Lett.* 43 (23), 12,071–12,081.
- Sugawara, T., 2000. Empirical relationships between temperature, pressure, and MgO content in olivine and pyroxene saturated liquid. *J. Geophys. Res.* 105 (B4), 8457–8472.
- Tenner, T.J., Hirschmann, M.M., Withers, A.C., Hervig, R.L., 2009. Hydrogen partitioning between nominally anhydrous upper mantle minerals and melt between 3 and 5 GPa and applications to hydrous peridotite partial melting. *Chem. Geol.* 262 (1–2), 42–56.
- Thoraval, C., Demouchy, S., 2014. Numerical models of ionic diffusion in one and three dimensions: application to dehydration of mantle olivine. *Phys. Chem. Miner.* 41 (9), 709–723. <https://doi.org/10.1007/s00269-014-0685-x>.
- Toramaru, A., 2006. BND (bubble number density) decompression rate meter for explosive volcanic eruptions. *J. Volcanol. Geotherm. Res.* 154 (3–4), 303–316.
- Toramaru, A., Noguchi, S., Oyoshihara, S., Tsune, A., 2008. MND (microlite number density) water exsolution rate meter. *J. Volcanol. Geotherm. Res.* 175 (1–2), 156–167.
- Turner, S., Black, S., Berlo, K., 2004. 210Pb–226Ra and 228Ra–232Th systematics in young arc lavas: implications for magma degassing and ascent rates. *Earth Planet. Sci. Lett.* 227, 1:1–16. <https://doi.org/10.1016/j.epsl.2004.08.017>.
- Van Hinsberg, V., Berlo, K., Migdisov, A., Williams-Jones, A., 2016. CO<sub>2</sub>-fluxing collapses metal mobility in magmatic vapour. *Geochem. Perspect. Lett.* 824 (LA-UR-15-28200).
- Wallace, P.J., Anderson Jr., A.T., 1998. Effects of eruption and lava drainback on the H<sub>2</sub>O contents of basaltic magmas at Kilauea Volcano. *Bull. Volcanol.* 59 (5), 327–344.
- Wilson, L., Head, J.W., 1981. Ascent and eruption of basaltic magma on the Earth and Moon. *J. Geophys. Res. Solid Earth* 86 (B4), 2971–3001. <https://doi.org/10.1029/JB086iB04p02971>.
- Witham, F., Blundy, J., Kohn, S.C., Lesne, P., Dixon, J., Churakov, S.V., Botcharnikov, R., 2012. SolEx: a model for mixed COHSCl-volatile solubilities and exsolved gas compositions in basalt. *Comput. Geosci.* 45, 87–97.
- Withers, A.C., Bureau, H., Raepsaet, C., Hirschmann, M.M., 2012. Calibration of infrared spectroscopy by elastic recoil detection analysis of H in synthetic olivine. *Chem. Geol.* 334, 92–98.
- Zhang, Y., Xu, Z., Zhu, M., Wang, H., 2007. Silicate melt properties and volcanic eruptions. *Rev. Geophys.* 45 (4). <https://doi.org/10.1029/2006rg000216> n/a-n/a.
- Zimmer, M.M., Plank, T., Hauri, E.H., Yogodzinski, G.M., Stelling, P., Larsen, J., Singer, B., Jicha, B., Mandeville, C., Nye, C.J., 2010. The role of water in generating the calc-alkaline trend: new volatile data for aleutian magmas and a new tholeiitic index. *J. Petrol.* 51 (12), 2411–2444. <https://doi.org/10.1093/ptrology/egq062>.
- Zussman, J., Howie, R., Deer, W., 1992. *An Introduction to the Rock Forming Minerals*. Longman Group Ltd, New York.